

# Observed and simulated inter-decadal changes in the structure of Southern Hemisphere large-scale circulation

Ana C. V. Freitas · Jorgen S. Frederiksen ·  
Jennifer Whelan · Terence J. O’Kane · Tércio Ambrizzi

Received: 30 May 2014 / Accepted: 9 February 2015 / Published online: 20 February 2015  
© Springer-Verlag Berlin Heidelberg 2015

**Abstract** Several studies have identified that, in the mid-1970s to early 1980s, a major shift occurred in the structure of the large-scale circulation in both hemispheres. This work employs the CSIRO Mk3L general circulation model in ensemble simulations with observed sea surface temperatures (SSTs) and historical time-evolving carbon dioxide (CO<sub>2</sub>) concentrations to investigate the inter-decadal changes found observationally in the jet streams, temperature, Hadley circulation, mean sea level pressure and precipitation. First, the performance of the model in simulating these changes for the mean July climate fields of 1949–1968 and 1975–1994, in comparison with the corresponding observations (NCEP/NCAR Reanalysis I and the Twentieth Century Reanalysis V2), is investigated. We find that the model is quite skilful in reproducing the broad features of the important inter-decadal changes that occurred in the mid-1970s. The model simulations and the NCEP/NCAR and twentieth century reanalyses agree in the eastern hemisphere; whereas in the western hemisphere the reanalyses show differences, and the simulations combine aspects of these two datasets. The role of the direct radiative forcing due to CO<sub>2</sub> in driving the inter-decadal changes is also examined. Results indicate that, in comparison with the indirect effect of CO<sub>2</sub> carried by the changing SSTs,

there is little additional impact of the direct radiative forcing due to CO<sub>2</sub> on the changes in the latter period. However, our simulations with fixed CO<sub>2</sub> concentration have shown clearly that the atmospheric simulations with historical time-evolving CO<sub>2</sub> concentrations are more skilful in reproducing the inter-decadal changes. The sensitivity of the ensemble results to employing the same or different time evolving sea ice boundary conditions in the ensemble members is also studied. The contributions of internal and external variability are discussed.

**Keywords** Jet streams · Hadley circulation · Temperature · Mean sea level pressure · Precipitation

## 1 Introduction

Atmospheric and oceanic large-scale circulation processes and their interactions play a key role in the climate system. Since the mid-1970s to early 1980s, the structure of the large-scale circulation in both hemispheres has exhibited prominent changes, contributing to coherent patterns of precipitation and temperature anomalies worldwide. Specifically in the Southern Hemisphere (SH), Frederiksen and Frederiksen (2005, 2007—hereafter FF05, FF07 respectively) found quite large changes in thermal structure and atmospheric circulation between the periods of 1949–1968 and 1975–1994. Their study was motivated by the dramatic reduction in average winter rainfall in the southwest of Western Australia (SWWA) that occurred after the mid-1970s (Allan and Haylock 1993; Hope et al. 2006; Pezza et al. 2008; Pook et al. 2012). FF05 and FF07 found a significant warming of the SH troposphere south of 30°S in the period 1975–1994, resulting in a reduction of the equator-to-pole temperature gradient. This in turn resulted in a

---

A. C. V. Freitas (✉) · T. Ambrizzi  
Institute of Astronomy, Geophysics and Atmospheric Sciences,  
University of Sao Paulo, São Paulo, SP 05508-090, Brazil  
e-mail: anacarolina@model.iag.usp.br

J. S. Frederiksen · J. Whelan  
CSIRO Oceans and Atmosphere Flagship,  
Aspendale, VIC, Australia

T. J. O’Kane  
CSIRO Oceans and Atmosphere Flagship, Hobart, TAS, Australia

17 % reduction in the peak strength of the SH subtropical jet stream over Australia and a reduction in the growth rates of storms, which led to the rainfall reduction in the SWWA. Between the periods of 1949–1968 and 1975–1994, there were also changes in the static stability (FF05, FF07), in the latitude of the high pressure belt, and in the eddy fluxes of heat and momentum (Zidikheri and Frederiksen 2013). Nitta and Yamada (1989) pointed out that the tropical sea surface temperature (SST), especially in central and eastern Pacific and in the Indian Ocean, has increased since the late 1970s. Corresponding to this tropical SST increase, the convective activity subsequently enhanced in the 1980s. Over the same period, O’Kane et al. (2013a) identified secular trends in the frequency of SH circulation regimes associated with the hemispheric wave three and blocking and the positive phase of the Southern Annular Mode.

The causes of observed atmospheric and oceanic circulation shifts since the mid-1970s are a subject of ongoing research, particularly whether they are a response to slowly varying external boundary forcing and radiative forcing (the externally forced component) or an expression of natural climate variability exhibited by the chaotic atmospheric dynamics in the absence of external forcing (internal climate variability). For example, Tett et al. (1999) found a global-mean temperature increase of approximately 0.6 K since 1900, occurring from 1910 to 1940 and from 1970 to the present. The authors state that the temperature change from 1970 is unlikely to be entirely due to internal climate variability and it has been attributed to changes in the concentrations of greenhouse gases and sulphate aerosols due to human activity. A similar conclusion was noted by Meehl et al. (2004), who found that the rapid increase of the surface air temperature since the mid-1970s had a substantial contribution from the anthropogenic forcing. Meehl et al. (2009) examined the significant shift from cooler to warmer tropical Pacific SSTs, which occurred in the mid-1970s, with effects that extended globally. The authors found that this observed 1970s climate shift had a contribution from changes in external forcing superimposed on what was likely an inherent decadal fluctuation of the Pacific climate system. O’Kane et al. (2013a) employed non-stationary time series analysis and Markov models to compare observations, reanalysis and simulations of the Atmospheric Model Inter-comparison Project, and showed that the secular trends in blocking and the Southern Annular Mode were not attributable to intrinsic variability.

Atmospheric model simulations with prescribed SST are extremely useful because they allow a distinction between the externally forced components and the internal variability of the atmospheric responses. An atmospheric variable is composed of two parts. One is the response of the atmosphere forced by SST, taken to be the same for each

atmospheric general circulation model (AGCM) ensemble member. The other is the internal variability of the atmosphere, and is different for each member. The SST-forced response is obtained as the average of the AGCM ensemble members. The internal variability in each AGCM ensemble member is defined by subtracting the SST-forced response (Chen et al. 2013). As noted by Rowell (1998), it is clearly important to be able to assess where on the globe atmospheric variations are sufficiently affected by oceanic forcing to enable practical seasonal prediction. This requires estimates of atmospheric potential predictability (Rowell et al. 1995; Rowell 1998). The potential predictability is defined as the ratio between the externally forced SST signal specified by inter-annual ensemble mean variance and the internal noise calculated by inter-ensemble variance (Shukla 1981; Rowell et al. 1995; Rowell 1998).

Folland et al. (1998) were the first to introduce an approach to climate change detection and attribution, which consists of integrations with an AGCM forced with the observed time-evolving SST and radiative forcing. This approach does not “double count” the atmospheric radiative forcing because only the direct effect is specified, whereas the indirect effect is included in the prescribed SST forcing (Deser and Phillips 2009). This methodology has been used to understand future projections of atmospheric circulation change (e.g. Cash et al. 2005; Stephenson and Held 1993) and assesses the relative roles of oceanic and direct atmospheric radiative forcings in driving the climate shift over the second half of the twentieth century (e.g. Deser and Phillips 2009; Bracco et al. 2004). However, most of these studies investigated the climate shift for boreal winter.

Grimm et al. (2006) demonstrated that some global climate models forced by SST may not be able to reproduce the inter-decadal changes in the basic state of the atmosphere. Thus, the first objective of this paper is to examine the extent to which atmospheric simulations by the CSIRO Mk3L model (Phipps 2010) with observed time-evolving SSTs and anthropogenic carbon dioxide (CO<sub>2</sub>) forcing are skilful in reproducing some of the important inter-decadal changes found in FF05 and FF07. We focus on the July climate fields for the two periods (1949–1968) and (1975–1994) and use both the National Centres for Environmental Prediction/National Center for Atmospheric Research (NCEP/NCAR) reanalysis and the twentieth century Reanalysis Version 2 (20CRV2) dataset. Atmospheric simulations with fixed and time-varying CO<sub>2</sub> concentrations are contrasted to examine the role of the direct radiative forcing due to CO<sub>2</sub> in driving the inter-decadal changes. Although part of the effects of time-varying CO<sub>2</sub> concentrations may be implicitly included in the SST signal (the indirect effect), we want to assess, at least qualitatively, the impact of the additional direct CO<sub>2</sub> forcing on the atmospheric circulation.

The CSIRO Mk3L employs a multi-layer dynamic-thermodynamic sea ice model, which means that the simulations considered here are forced with the same observed time-evolving SSTs and CO<sub>2</sub> concentrations, but not the same sea ice boundary conditions. Thus, we investigate if the simulated inter-decadal changes are different if each ensemble member is forced with the same time-evolving sea ice boundary conditions in each realization. Additionally, we investigate the inter-annual and inter-decadal changes observed in the SSTs. Finally we quantify the model's potential predictability on monthly, seasonal and inter-decadal time scales.

In summary, the goal of our study is to address the following questions:

1. Are the inter-decadal changes found in FF05 and FF07 mainly using NCEP/NCAR reanalysis also observed in the 20CRV2 dataset and in our model simulations?
2. How realistic are the simulated inter-decadal changes when forced with the combined observed evolution of SST forcing and CO<sub>2</sub> radiative forcing?
3. How different are the simulated inter-decadal changes when forced with fixed and time-evolving CO<sub>2</sub> concentrations?
4. What is the role of the direct radiative forcing due to CO<sub>2</sub> and what are the contributions of forced and unforced (internal variability) components in driving the climate shift?
5. How different are the simulated inter-decadal changes when forced with the same sea ice boundary conditions?
6. What are the inter-annual and inter-decadal changes observed in the SSTs and how are they related to changes in the CO<sub>2</sub> forcing?

The paper is organized as follows. The observational datasets, model simulations and methodology are described in Sect. 2. The two first questions (1)–(2) cited above are addressed in Sect. 3, where we analyse mainly the performance of the model, with the combined observed evolution of SST and CO<sub>2</sub> forcings, in simulating the inter-decadal changes found observationally in the jet streams, temperature, Hadley circulation, mean sea level pressure and precipitation. The other questions are addressed in Sect. 4. Finally, discussion and conclusions highlighting the main results of the paper are presented in Sect. 5.

## 2 Data and methods

### 2.1 Reanalyses datasets

Reanalyses datasets optimally combine numerical weather prediction model output with assimilated data from

different observational data platforms in order to provide information in otherwise data-sparse regions. Such model-data syntheses afford our best estimate of the time evolving state of the atmosphere over the recent past.

The air temperature, mean sea level pressure, zonal and meridional wind monthly data were obtained from the NCEP/NCAR Reanalysis I<sup>1</sup> (Kalnay et al. 1996) on a 2.5° latitude by 2.5° longitude grid at 17 pressure levels and from the 20CRV2<sup>2</sup> (Compo et al. 2011) on a 2.0° latitude by 2.0° longitude grid at 24 pressure levels. The 20CRV2 utilizes a new version of the NCEP atmosphere–land model with interpolated monthly SST and sea-ice concentration fields from the Hadley Centre Global Sea Ice and Sea Surface Temperature (HADISST) dataset as prescribed boundary conditions, newly compiled surface pressure observations, and the radiative effects of historical time-varying CO<sub>2</sub> concentrations, volcanic aerosol and solar variations to produce a reanalysis dataset spanning 1871 to the present (Compo et al. 2011).

Our results will show that, for the periods considered in this work, the model simulations, and the NCEP/NCAR and 20CRV2 reanalyses, agree in the eastern hemisphere, but in the western hemisphere, the reanalyses show significant differences with the model simulations combining aspects of these two datasets. Differences between the reanalyses, especially in the vertical structure, may be attributed to differences in the data assimilation techniques utilized. For the 20CRV2 dataset only surface pressure observations are assimilated while for the NCEP/NCAR reanalysis other available atmospheric fields have also been employed.

One possible concern is the change in the quantity and spatial coverage of the observed data included in the reanalyses, since the evolution of the global observing system has three major phases: the “early” period, from the 1940s to the International Geophysical Year in 1957, when the first upper-air observations were established; the “modern rawinsonde network” from 1958 to 1978; and the “modern satellite” era from 1979 to the present (Kistler et al. 2011). Specifically in the western part of the SH there were few observations before 1979 and the 20CRV2 has an extremely limited station network in this region prior to about 1960, particularly in the Pacific sector.<sup>3</sup> However, FF07 performed sensitivity studies to the choice of basic states based on the NCEP/NCAR reanalysis and the European Centre for Medium Range Weather Forecasting (ECMWF)

<sup>1</sup> NCEP/NCAR Reanalysis I is available on: <http://www.cdc.noaa.gov/cdc/reanalysis>.

<sup>2</sup> Twentieth century reanalysis version 2 is available on: [http://www.esrl.noaa.gov/psd/data/gridded/data.20thC\\_ReanV2.html](http://www.esrl.noaa.gov/psd/data/gridded/data.20thC_ReanV2.html).

<sup>3</sup> Station network composition is available on: <ftp://ftp.ncdc.noaa.gov/pub/data/ispd/add-station/v4.0/>.

40 year reanalysis (ERA-40) and found remarkable consistency of the results for the inter-decadal changes analysed here.

## 2.2 Model details

This study employs the CSIRO Mk3L model version 1.2, which is a general circulation model designed for the study of climate variability and change on monthly to millennial timescales (Phipps 2010; Phipps et al. 2011, 2013). The atmospheric component of Mk3L is based on the CSIRO Mk3 model (Gordon et al. 2002) with rhomboidal 21 resolution. A hybrid vertical coordinate is used, with 18 vertical levels. The model incorporates both a cumulus convection scheme (Gregory and Rowntree 1990) and a prognostic stratiform cloud scheme (Rotstajn 1997, 1998, 2000). Time integration is via a semi-implicit leapfrog scheme, with a Robert–Asselin time filter (Robert 1966) used to prevent decoupling of the time-integrated solutions at odd and even timesteps. The Mk3L atmosphere model uses a timestep of 20 min.

The atmospheric component consists of equations for atmospheric transport, radiative exchange, convection and clouds. The radiation calculations treat longwave and shortwave radiation separately, and include the effects of CO<sub>2</sub>, ozone, water vapour and clouds. Climatological values of the ozone concentrations are taken from the Atmospheric Model Intercomparison Project (AMIP II) recommended dataset (Wang et al. 1995). A multi-layer dynamic-thermodynamic sea ice model and a land surface model are included. In the stand-alone atmosphere model, the temperatures of the sea gridpoints are determined by the monthly-mean observed SSTs. Linear interpolation in time is used to estimate values at each timestep, with no allowance for diurnal variation.

## 2.3 Atmosphere model simulations

A set of thirteen numerical simulations forced by the observed monthly mean HADISST dataset (Rayner et al. 2003)<sup>4</sup> from 1870 to 2010 and historical time-evolving CO<sub>2</sub> concentrations have been conducted (hereafter denoted TRANSIENT ensemble). The ensemble members are constructed by perturbing the initial conditions, which allows us to separate the “SST-forced” (or external) response from variability that arises from processes internal to the atmosphere (Rowell et al. 1995; Rowell 1998). The Mk3L standard or default initial conditions are obtained from a 100 year spin-up run in which the atmosphere-land-sea ice

model is integrated to equilibrium for pre-industrial conditions (Phipps 2010). The pre-industrial conditions are specified by climatological SSTs and CO<sub>2</sub> concentration fixed at 280 ppm. The state of the system at the end of this spin-up run is saved as the default restart file; it contains the default initial condition information for restarting the model.

The first transient simulation, initialized from the Mk3L atmosphere-land-sea ice model default restart file and forced by time-varying observed SSTs and time-evolving CO<sub>2</sub> concentrations, is our Standard Transient run (denoted STD-TRANSIENT run). To generate the other twelve ensemble members, four restart files are obtained from the last years of a control run, also initialized from the Mk3L default restart file and performed for 145 years under constant pre-industrial boundary conditions (climatological SSTs and CO<sub>2</sub> concentration fixed at 280 ppm). Four simulations are initialized directly from these four restart files. The last eight simulations are initialized from eight restart files generated through perturbations to the four restart files according to following equation, applied only to the atmospheric fields (pressure, streamfunction, velocity potential, temperature):

$$NRF = DRF \pm [(DRF - FRF) * 0.1] \quad (1)$$

Here, NRF is the new restart file generated for each of the last eight simulations, DRF is the default restart file used in the control run and in the STD-TRANSIENT simulation and FRF is any of the four restart files cited above, which were obtained from the control run. As we will show below, the STD-TRANSIENT simulation skilfully reproduces the broad features of the observations and, because of this, we choose to initiate the last eight simulations by varying slightly the atmospheric fields of the DRF, according to Eq. (1), and leaving unchanged the other variables present in this file.

In summary, the TRANSIENT ensemble consists of the standard member, STD-TRANSIENT, which starts from the default restart file, and twelve perturbed members with initial conditions described above.

To assess the sensitivity of the results to the choice of the time-varying external forcing, thirteen additional simulations have been conducted using the same parameters described above, but with fixed CO<sub>2</sub> concentration at 348 ppm (hereafter denoted the 348PPM ensemble), as in Meng et al. (2012). For comparison purposes, further explained in the Sect. 4.1, thirteen simulations at 300 ppm concentration (hereafter denoted the 300 PPM ensemble) have also been conducted. Table 1 provides a summary of the experiments performed in this study.

It is important to highlight that the atmospheric simulations considered in this work incorporate the results of the multi-layer dynamic-thermodynamic sea ice model, and

<sup>4</sup> HADISST dataset is available on: <http://www.metoffice.gov.uk/hadobs/hadisst/data/download.html>.

**Table 1** List of the experiments performed with the Mk3L stand-alone atmosphere model

Experiment name	Carbon dioxide concentration	SST boundary forcing	Run period	Restart files
STD-TRANSIENT run	Time-evolving	Time-evolving	1870–2010	1 from default
Control run	Fixed at 280 ppm	Climatological	145 years	1 from default
TRANSIENT ensemble (13 members)	Time-evolving	Time-evolving	1870–2010	1 from default, 4 from control run and 8 from Eq. (1)
348PPM ensemble (13 members)	Fixed at 348 ppm	Time-evolving	1870–2010	1 from default, 4 from control run and 8 from Eq. (1)
300PPM ensemble (13 members)	Fixed at 300 ppm	Time-evolving	1870–2010	1 from default, 4 from control run and 8 from Eq. (1)
SAME-ICE ensemble (13 members)	Time-evolving	Time-evolving but same daily sea ice values from STD-TRANSIENT run	1870–2010	1 from default, 4 from control run and 8 from Eq. (1)

therefore are not forced by the observed monthly mean HADISST sea ice dataset (Rayner et al. 2003). However, the simulated sea ice concentration (for the TRANSIENT ensemble mean) captures very well the observed concentration (HADISST dataset) with a correlation of 0.8 for the difference between the two periods (1975–1994) and (1949–1968). One could argue that the results found in this work might be different if the construction of the ensemble members had considered the same time evolving sea ice boundary condition in each realization. This hypothesis has been tested by repeating the TRANSIENT ensemble but imposing for the sea ice concentration the same daily values calculated by the sea ice model in the STD-TRANSIENT run. The results obtained with these simulations (hereafter denoted the SAME-ICE) are discussed in Sect. 4.

All simulations considered here use a prescribed ozone climatology taken from the AMIP II recommended dataset (Wang et al. 1995). However, the radiation scheme in Mk3L does not account for the radiative effects of methane, nitrous oxide or chlorofluorocarbons. Therefore, we cannot exclude the possibility that the observed inter-decadal changes are not fully captured by the model partly because other greenhouse gases, as well as other natural and anthropogenic forcings, are not explicitly included in the simulations considered in this study.

### 3 Assessing the skill of Mk3L stand-alone atmospheric model

This section focuses on some important inter-decadal changes found by FF05 and FF07 in the jet streams, temperature, Hadley circulation, mean sea level pressure and precipitation. The model results for each one of these atmospheric fields are presented in the following subsections. We have focused on the difference between July climate fields in the two periods (1975–1994) and (1949–1968), since it portrays the changes that occurred in the

mid-1970s. Although these changes can be also verified for the June–July–August (JJA) mean, their magnitudes are greater for the month of July.

As noted by Frederiksen et al. (2011), even for climate averages computed over a 20-year period, there may be considerable variability in simulations by different models or members from the same model. Further, ensemble means will tend to have less spatial variability (reduced troughs and peaks) than individual members or the reanalyses because of phase shifts in the responses of the members. In this section, we first focus mainly on the results of the STD-TRANSIENT run with default initial conditions and then, in Sect. 4, we consider the results for the TRANSIENT ensemble mean. The STD-TRANSIENT run is representative of the more skilful members and reproduces many of the broad features of the observed changes between (1949–1968) and (1975–1994) quite well. It also displays the main features of the TRANSIENT ensemble, but the magnitudes of the inter-decadal changes in the ensemble average are smaller.

#### 3.1 Jet streams

Figure 1 shows the vertical cross-section of July zonal wind, averaged over 100°E–130°E longitude, for the NCEP/NCAR reanalysis (as in FF05), the STD-TRANSIENT run and the 20CRV2 dataset. This longitude band is where the magnitude of the changes in the subtropical jet and baroclinicity are largest; it is also most relevant to changes in SWWA rainfall (FF05, FF07). At about 200 hPa, the maximum in the zonal wind strength near 30°S for the 1949–1968 basic state is reproduced by the STD-TRANSIENT simulation with slightly overestimated values (Fig. 1b) compared to the NCEP/NCAR reanalysis (Fig. 1a) and to the 20CRV2 (Fig. 1c).

FF05 and FF07 found, for the latter period (1975–1994), a reduction in the zonal wind near 30°S in the upper troposphere and, an increase near 45°S and in the main NH jet

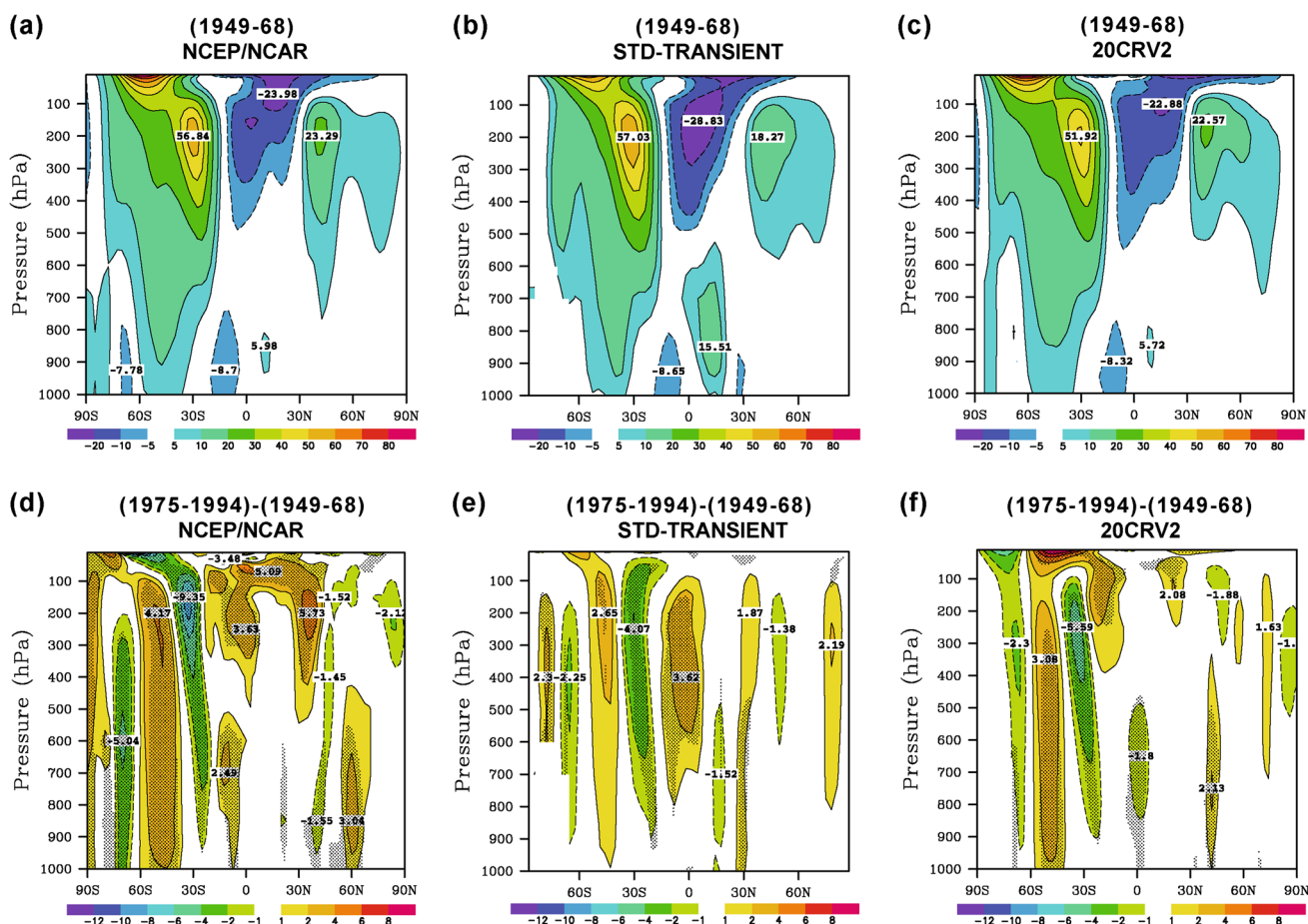


**Fig. 1** Vertical cross-section of July zonal wind ( $\text{m s}^{-1}$ ), averaged over  $100^{\circ}$ – $130^{\circ}\text{E}$  longitude, as a function of latitude and pressure (hPa) for the 1949–1968 basic state, and for the difference (1975–1994) to (1949–1968). Plots **a**, **d** for NCEP/NCAR data as in FF05. Plots **b**, **e** for the STD-TRANSIENT run and **c**, **f** for the 20CRV2

data. Contour intervals are  $10 \text{ m s}^{-1}$  for the 1949–1968 basic state and  $2 \text{ m s}^{-1}$  for the difference (1975–1994)–(1949–1968) with stippling indicating regions where the differences are statistically significant at the 95 % level as determined by Student's *t* test. Negative (positive) values are indicated by *dashed* (*solid*) lines

core near  $35^{\circ}\text{N}$  (Fig. 1d, as in FF05). The STD-TRANSIENT run is quite skilful in reproducing the broad structures of these changes, although it underestimates the magnitude in the SH (Fig. 1e) compared to the reanalyses (Fig. 1d, f). The 20CRV2 also shows the changes in the SH jet streams (Fig. 1f), with reduced magnitude compared to the NCEP/NCAR reanalysis (Fig. 1d). The increase in the main NH jet core near  $35^{\circ}\text{N}$  in the upper troposphere is not observed in the 20CRV2 (Fig. 1f).

In the SH lower stratosphere there are differences between the reanalyses (Fig. 1d, f). According to the National Oceanic & Atmospheric Administration (NOAA) website,<sup>5</sup> verification tests have shown that the 20CRV2 dataset, constructed with only surface pressure observations, creates reasonable atmospheric fields up to the

tropopause; this means that the data are probably less reliable above the tropopause, which might explain the differences between the reanalyses in the SH lower stratosphere.

To investigate the quantitative agreement between the model simulations and reanalysis results in Fig. 1, correlation coefficients calculated for each pressure level in the month of July have been displayed in Fig. 2. For the 1949–1968 basic state (Fig. 2a), the STD-TRANSIENT run and the TRANSIENT ensemble mean have correlations larger than 0.95 with the NCEP/NCAR reanalysis from 70 to 10 hPa while from 400 to 100 hPa the correlations are larger than 0.95 with both reanalyses. Figure 2b shows that, for the difference between the two periods [(1975–1994)–(1949–1968)], the STD-TRANSIENT run and the TRANSIENT ensemble mean has correlations above 0.64 with the NCEP/NCAR reanalysis from 600 to 200 hPa. In general, the model simulations have larger correlations with the NCEP/NCAR reanalysis.

<sup>5</sup> <http://www.esrl.noaa.gov/psd/data/testdap/datasets.html>.

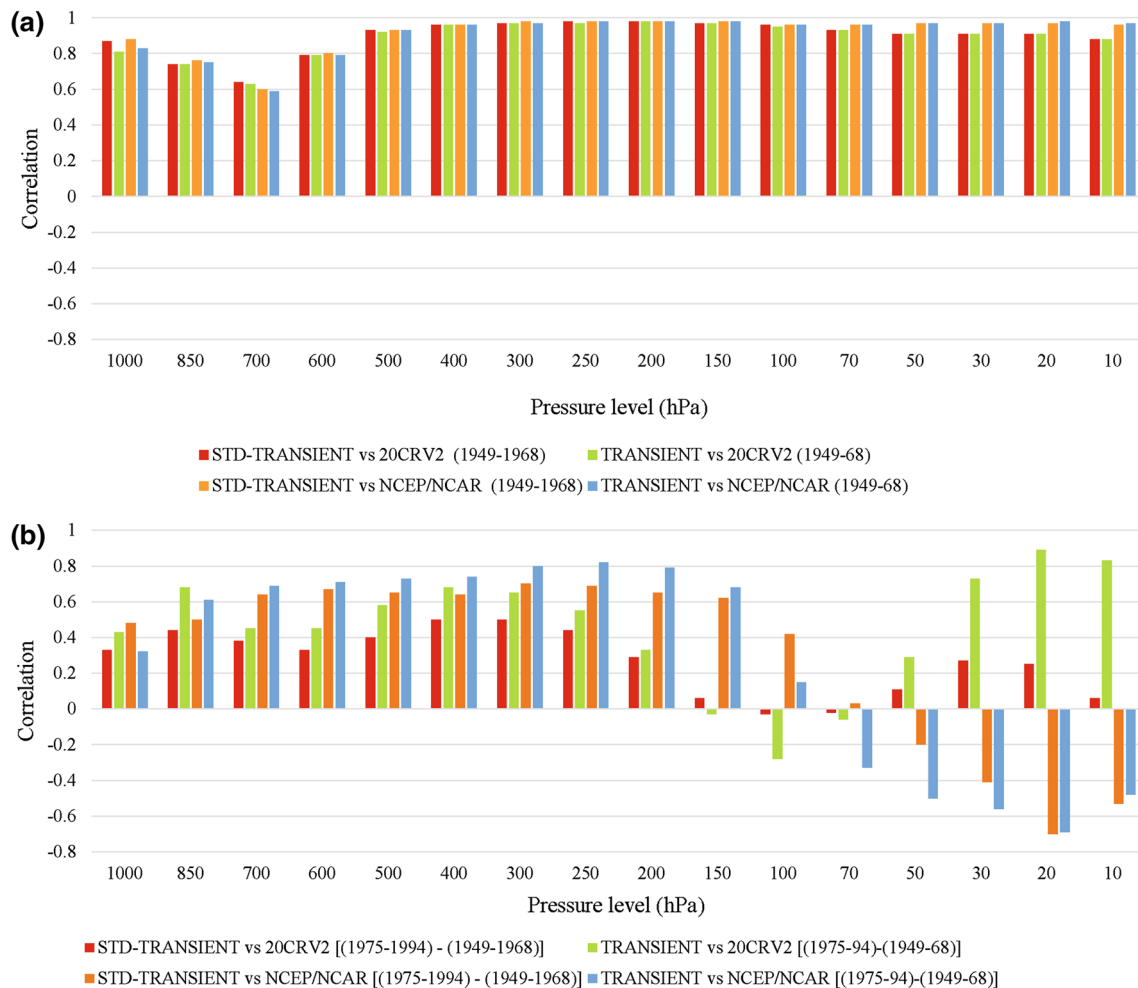


**Fig. 2** Pearson correlation coefficients as a function of pressure level between CSIRO Mk3L atmospheric model (TRANSIENT ensemble mean and STD-TRANSIENT run) and reanalyses (NCEP/NCAR and 20CRV2) for the vertical cross-section of July zonal wind averaged

between  $100^{\circ}$  and  $130^{\circ}$ E for **a** the 1949–1968 period and **b** the difference (1975–1994)–(1949–68). Values greater than 0.444 or less than  $-0.444$  are statistically significant at the 95 % level

Regarding to the longitudinal variations in the jet streams, FF05 and FF07 found that the reduction in the zonal wind in the 1975–1994 period extends across essentially the whole hemisphere in a band centred near  $30^{\circ}$ S at 300 hPa. FF05 and FF07 also found a band to the south centred near  $50^{\circ}$ S with increases in the zonal wind up to  $5.6 \text{ ms}^{-1}$ . These findings were also noted by Archer and Caldeira (2008), who analysed historical trends of jet stream properties based on the ERA-40 and the NCEP/NCAR reanalysis datasets for the period 1979–2001, and Pena-Ortiz et al. (2013) using a 3-D jet streaks detection algorithm with NCEP/NCAR reanalysis data. Figure 3a shows these changes in the jet streams based on the NCEP/NCAR reanalysis. The 20CRV2 (Fig. 3c) and the STD-TRANSIENT run (Fig. 3b) show broadly similar changes to the NCEP/NCAR reanalysis in the eastern hemisphere but different patterns of zonal wind changes in the western

hemisphere. From  $90^{\circ}$  to  $150^{\circ}$ E longitude and from  $30^{\circ}$  to  $90^{\circ}$ S latitude the STD-TRANSIENT simulation and both reanalyses show very similar changes, although with some differences in magnitude. In the western hemisphere, the STD-TRANSIENT run results agree more closely with the 20CRV2 dataset, showing a similar pattern for the zonal wind changes, especially in the Atlantic Ocean for middle and high latitudes and around  $150^{\circ}$ W from  $0^{\circ}$  to  $40^{\circ}$ S (Fig. 3b, c).

### 3.2 Temperature

FF05 and FF07 found that the thermal structure of the SH atmosphere had changed between (1949–1968) and (1975–1994) with significant warming south of  $30^{\circ}$ S, leading to a reduced equator-to-pole temperature gradient, particularly in the eastern hemisphere. As well, this reduction in

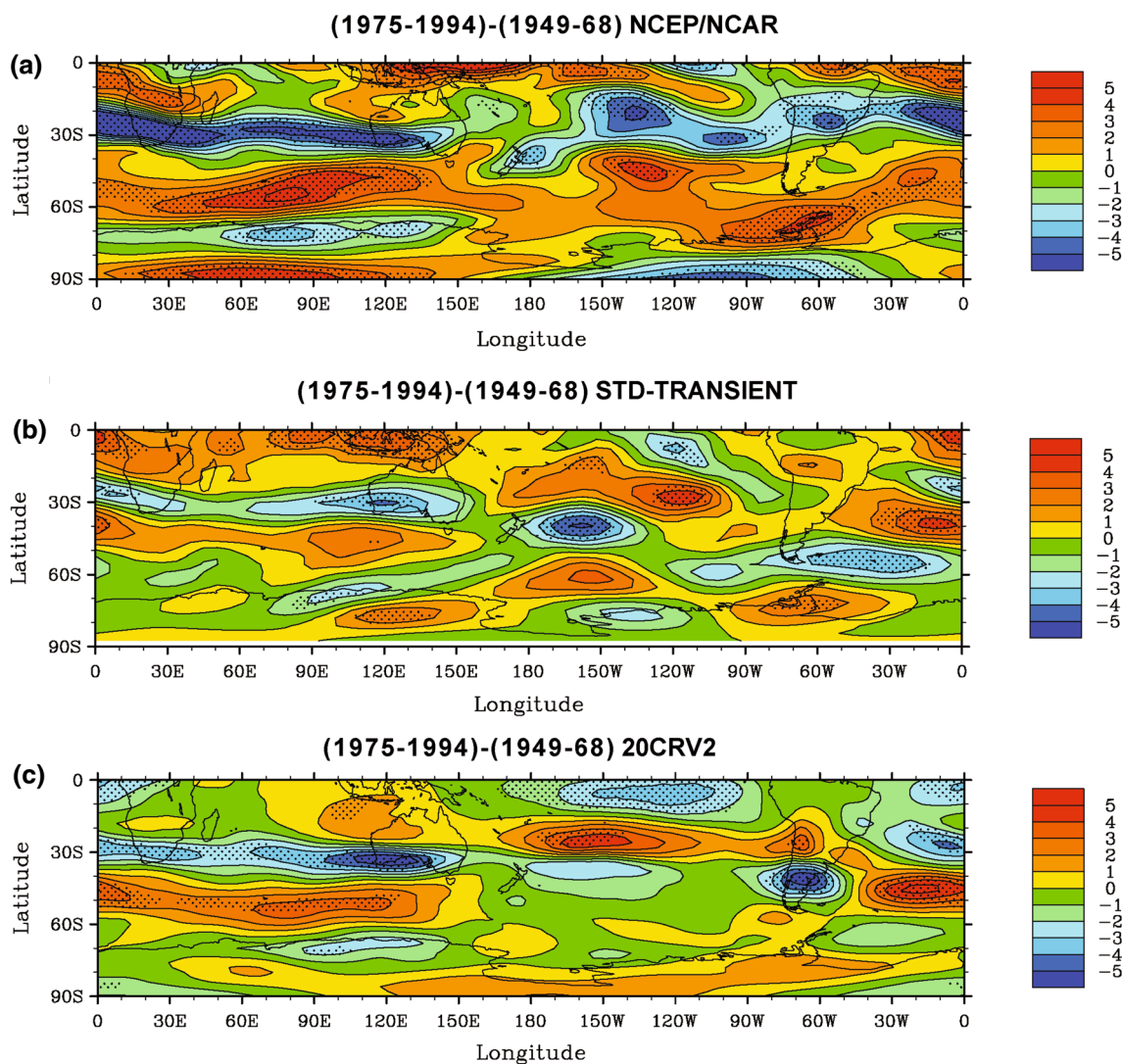


**Fig. 3** Zonal wind ( $\text{m s}^{-1}$ ) for July at 300 hPa for the difference (1975–1994)–(1949–1968). Plot **a** for the NCEP/NCAR data, **b** for the STD-TRANSIENT run and **c** for the 20CRV2 data. Contour inter-

vals are  $1 \text{ m s}^{-1}$  with stippling indicating regions where the differences are statistically significant at the 95 % level as determined by Student’s  $t$  test

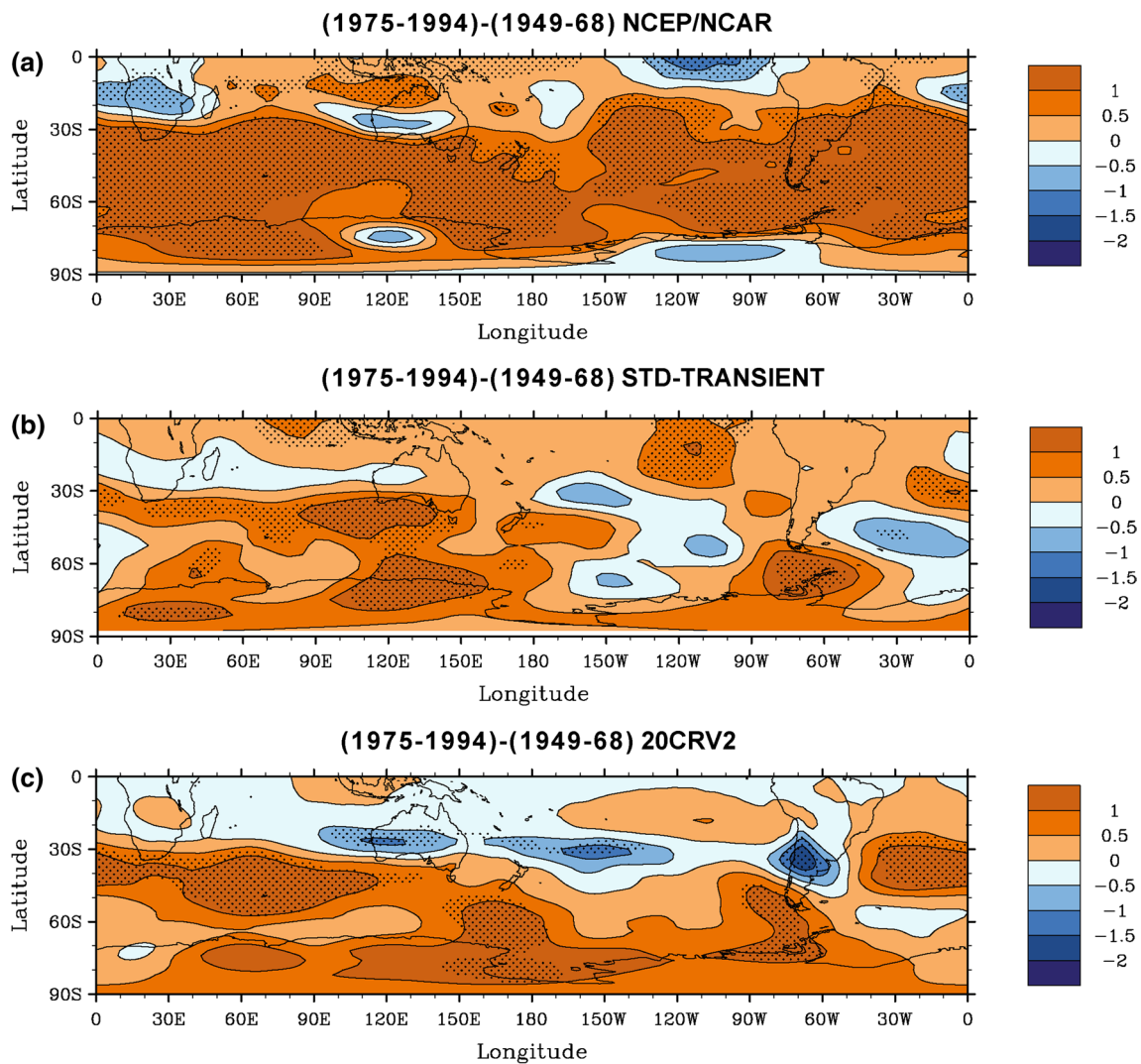
the atmospheric temperature gradient around  $30^\circ\text{S}$  is associated, by thermal wind balance, with the reduction in the vertical shear of the zonal wind.

Figure 4 shows the potential temperature at 500 hPa for the difference between the two periods. The potential temperature is defined by the following relationship:

$$\theta = T \left( \frac{p_s}{p} \right)^{R/c_p} \tag{2}$$

where  $R$  is the gas constant of air,  $c_p$  is the specific heat capacity at constant pressure and  $\theta$  is the temperature that a parcel of dry air at pressure  $p$  and temperature  $T$  would have if it were expanded or compressed adiabatically to surface pressure  $p_s$  (Holton 2004).

The significant warming south of  $30^\circ\text{S}$ , noted by FF05 and FF07 from the NCEP/NCAR reanalysis data (Fig. 4a), is captured by the STD-TRANSIENT run (Fig. 4b), although there is a cooling region around  $150^\circ\text{W}$ , south of  $30^\circ\text{S}$ . There are some differences between the reanalyses, especially in the western hemisphere and equatorward of  $30^\circ\text{S}$ , which may be attributed to differences in the data assimilation techniques utilized by them. However, the 20CRV2 also shows the significant warming south of  $30^\circ\text{S}$  (Fig. 4c). The cooling regions over Madagascar, South Africa and the west of Australia around  $20^\circ\text{S}$  are seen in both reanalyses (Fig. 4a, c) and in the STD-TRANSIENT simulation (Fig. 4b), since in the eastern hemisphere there is better agreement between the model simulations and the reanalyses. However, only the STD-TRANSIENT run



**Fig. 4** Potential temperature (K) for July at 500 hPa for the difference (1975–1994)–(1949–1968). Plot **a** for the NCEP/NCAR data, **b** for the STD-TRANSIENT run and **c** for the 20CRV2 data. Contour

intervals are 0.5 K with stippling indicating regions where the differences are statistically significant at the 95 % level as determined by Student’s *t* test

(Fig. 4b) and the 20CRV2 (Fig. 4c) show cooling regions over the central Indian Ocean around 20°S, over the Pacific Ocean around 30°S, from 180° to 120°W, and over the Atlantic Ocean around 60°S.

### 3.3 Hadley circulation

The Hadley cell is generally defined as the zonal mean meridional mass circulation in the atmosphere bounded roughly by 30°S and 30°N, with warmer air rising in the tropics and colder air sinking in the subtropics. This circulation is one of the fundamental regulators of the earth’s energy budget, transporting heat poleward and thus, reducing the resulting equator-to-pole temperature gradient. As well, the Hadley cell also transports momentum poleward, strongly influencing the subtropical jet streams. Thus, the

weakening of the Australian jet stream and the reduction of the equator-to-pole temperature gradient in the latter period discussed earlier are probably associated with alterations in the Hadley Circulation (HC), as found by FF05 and FF07.

The HC is described in terms of the mean meridional mass streamfunction  $\psi$  (Oort and Yienger 1996) computed using the zonal-mean meridional wind and the surface pressure according to the following equation:

$$\psi(\varphi, p) = \frac{2\pi a \cos\varphi}{g} \int_p^{p_s} [\bar{v}(p', \varphi)] dp' \tag{3}$$

Here *a* is the earth’s radius,  $\varphi$  is the latitude,  $\bar{v}$  is the zonally averaged temporal mean of the meridional velocity, *p* is the pressure, *p<sub>s</sub>* is the surface pressure, *g* is the acceleration of gravity. This formula quantifies air mass transport in

the tropics and subtropics and the strength or intensity of the HC is defined by the maximum value of the zonal mean meridional mass streamfunction. The HC poleward expansion is defined as the latitude at which the streamfunction takes the value 0.0, interpolated on the latitude grid, at the pressure level of 500 hPa (Gastineau et al. 2009).

Following the Oort and Yienger (1996) convention,  $\psi$  corresponding to a clockwise circulation is positive (as in the NH winter cell), whereas  $\psi$  corresponding to a counter-clockwise circulation (as in the SH winter cell) is negative. Thus, a strengthening of the SH HC corresponds to a negative value of the  $\psi$  change for the month of July.

Table 2 shows the mean SH HC intensity in the reanalyses and model simulations for the two periods analysed and for the difference between them. A weakening of the HC can be seen in the latter period (1975–1994) for the NCEP/NCAR reanalysis and the model simulations. However, no significant response is seen in the 20CRV2. As well, it is evident that the magnitude of the mean HC intensity for both periods is smaller for the NCEP/NCAR reanalysis, as also found in other studies (c.f. Figure 2, 6 and Table 2 of Stachnik and Schumacher 2011; Figure 3 of Lucas et al. 2014). Stachnik and Schumacher (2011), using the meridional streamfunction index, found significant variability in the long-term trends and climatology of HC intensity in recent decades among eight different reanalysis datasets. The ERA-40 exhibits one of the strongest circulations for the SH, whereas the NCEP/NCAR reanalysis is a more obvious weak outlier for the southern cell.

Another common index to study the HC intensity is the vertical shear of the zonally averaged meridional velocity between 200 and 850 hPa (Oort and Yienger 1996). Figure 5a shows this index in each period considered here for model simulations and reanalyses. We note that each dataset has a parabolic shape with a trough near the equator. The trough for the 20CRV2 dataset is deeper in the 1975–1994 period indicating a strengthening of the SH HC. A prominent

feature in Fig. 5 is the fact that the NCEP/NCAR reanalysis has a shallower trough for both periods compared with the 20CRV2 dataset and the TRANSIENT ensemble mean. As expected, these findings are in agreement with the earlier discussion based on the meridional streamfunction index (Table 2) since both are based on the meridional wind. It is also worth remembering that the HC is a zonal-mean quantity and, as previously discussed for the zonal wind and temperature fields, the reanalyses present significant differences in the western hemisphere. Figure 5b shows the difference between the two reanalyses for the meridional wind at 200 hPa [(1975–1949)–(1949–1968)]. There are significant differences between the reanalyses from 0 to 40°S in the western hemisphere (mainly over the Pacific and Atlantic Oceans) and thus, this reflects in the inconsistencies found for the HC intensity magnitude and changes in the latter period. In this context, Song and Zhang (2007) also found different trends in the SH winter HC intensity between the ERA-40 and the NCEP/NCAR reanalyses primarily over the western tropical oceans where few atmospheric radiosonde measurements exist. Both the NCEP/NCAR and ECMWF reanalyses used similar input data of operational radiosondes and satellite measurements, but the authors found significant differences in the HC intensity trend over the last 50 years. The 20CRV2 dataset assimilates only surface pressure observations and, therefore, there is a potential for large differences, especially in vertical structure, between this dataset and the NCEP/NCAR reanalysis. As well, the zonal mean HC represents an ageostrophic circulation, which is more difficult to capture in statistical or numerical approaches and thus, more subject to the vagaries of the reanalysis models.

We established earlier that, in the western hemisphere, the model simulations show better agreement with the 20CRV2 dataset for the zonal wind and temperature fields. Analysing the difference between the two reanalyses and the model simulations for meridional wind at 200 hPa [(1975–1949)–(1949–1968)], we found that the model simulations are in better agreement with the 20CRV2 dataset over the central Pacific around 15°S, over the western Pacific around 30°S, over the Atlantic Ocean around the equator and over the Maritime Continent region (Figure not shown). However, over the eastern Atlantic from 0 to 40°S and over the Atlantic Ocean and eastern Pacific around 35°S the model simulations are in better agreement with the NCEP/NCAR reanalysis (Figure not shown). These results indicate that the weakening of the HC, which was detected earlier only for the NCEP/NCAR and model simulations, may be attributed mainly to the changes in the regional HC in the 1975–1994 period. In this context, a weakening of the upper-level HC west of Africa in the 1971–2000 period was shown by Baines (2005).

In terms of trend, Table 3 shows a HC weakening trend for the whole period (1949–1994) in July and also in JJA for

**Table 2** Mean HC Intensity ( $\times 10^9$  kg s $^{-1}$ ) for the reanalyses and ensemble means analysed in the periods 1949–1968, 1975–1994, and the mean difference

Data/ simulation	1949–1968	1975–1994	Mean difference (95 % confidence interval)
NCEP/NCAR	–18.97	–17.72	<b>+1.25</b> (0.69 to 1.81)
20CRV2	–24.02	–24.56	–0.54 (–1.92 to 0.84)
TRANSIENT	–27.75	–26.93	<b>+0.82</b> (0.13 to 1.51)
348PPM	–27.65	–26.83	<b>+0.82</b> (0.13 to 1.52)
300PPM	–27.96	–27.17	<b>+0.79</b> (0.18 to 1.41)
SAME-ICE	–27.90	–26.92	<b>+0.98</b> (0.28 to 1.68)

Values in bold are statistically significant at 95 % level from Student's *t* test

+Difference signal indicates weakening of the HC in the latter period

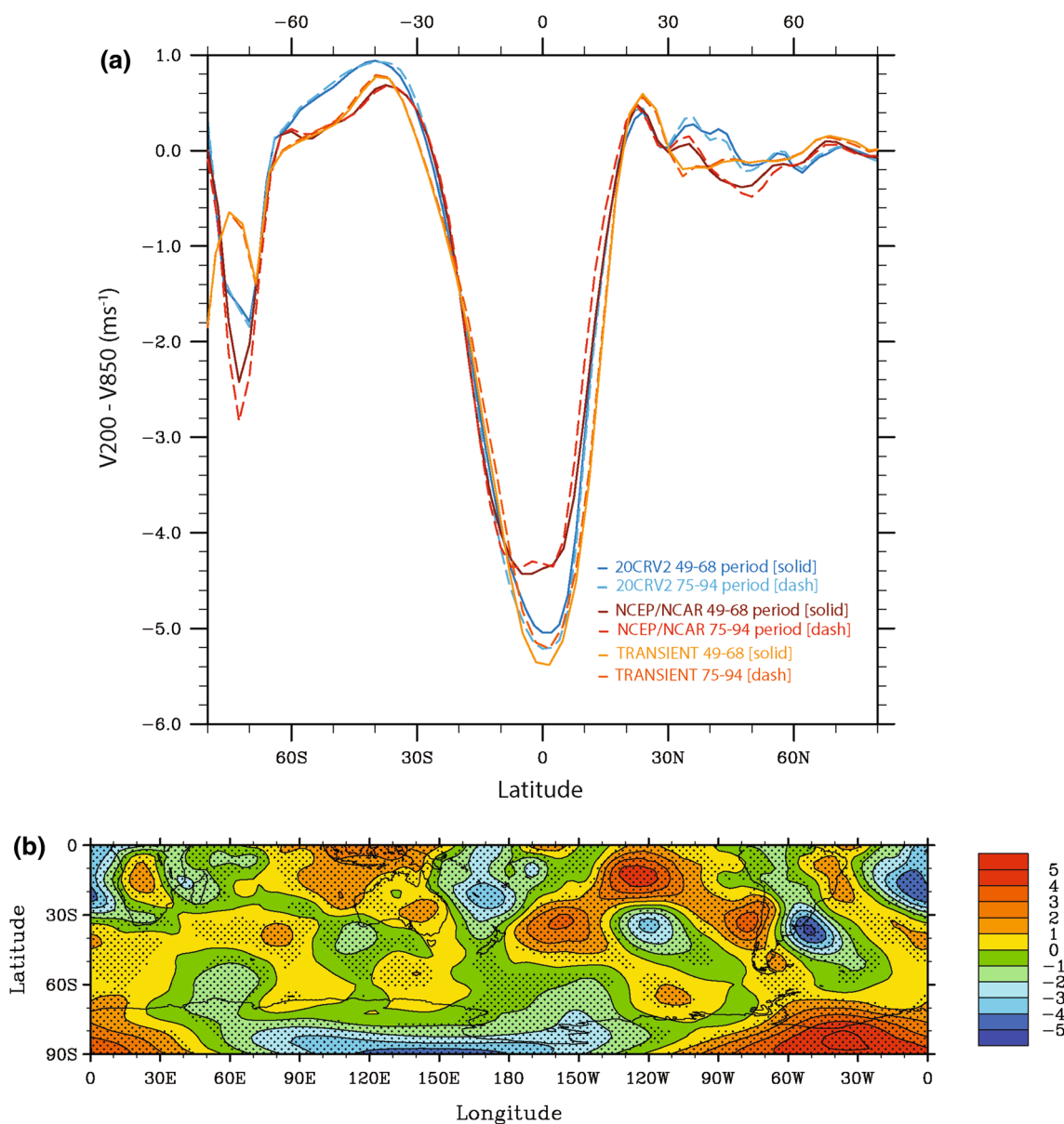


**Fig. 5** **a** July difference between the zonal mean of the meridional wind ( $\text{m s}^{-1}$ ) at 200 and 850 hPa for the 20CRV2 (blue lines), the NCEP/NCAR reanalysis (red lines) and the TRANSIENT ensemble mean (orange lines) for the 1949–1968 period (solid line) and for the 1975–1994 period (dashed line); **b** July meridional wind ( $\text{m s}^{-1}$ ) at

200 hPa for the difference 20CRV2 [(1975–1994)–(1949–1968)]–NCEP/NCAR reanalysis [(1975–1994)–(1949–1968)] with stippling indicating regions where the differences are statistically significant at the 95 % level as determined by Student’s *t* test

the NCEP/NCAR reanalysis and for the model simulations (significant only in JJA). However, strengthening trends of nearly equal magnitude are found for the 20CRV2 (significant only in JJA and more uncertain). The two reanalyses also show opposite latitudinal shifts of the HC in the latter period (1975–1994). There are significant linear trends for the period 1949–1994, with the NCEP/NCAR reanalysis (20CRV2) showing a HC poleward (equatorward) shift of 0.11 (0.33) degrees per decade for July and of 0.20 (0.17) degrees per decade for JJA. The HC poleward shift trend for

the model simulations is very small and not significant. Differences in the HC trends among reanalyses may be attributed to the fact that the 20CRV2 dataset assimilates only surface observations, as discussed earlier.

### 3.4 Mean sea level pressure

Sadler et al. (1988), Allan and Haylock (1993) and Smith et al. (2000) found that the dramatic reduction in winter rainfall in the SWWA is associated with an increase

**Table 3** Linear trend for the HC Intensity ( $\times 10^9 \text{ kg s}^{-1}$  per decade) in the 1949–1994 period for the reanalyses and ensemble means analysed

Data/simulation	Linear trend July 1949–1994 (95 % confidence interval)	Linear trend JJA 1949–1994 (95 % confidence interval)
NCEP/NCAR	<b>+0.36</b> (0.14 to 0.59)	<b>+0.35</b> (0.17 to 0.53)
20CRV2	−0.30 (−0.76 to 0.16)	− <b>0.34</b> (−0.009 to −0.67)
TRANSIENT	+0.16 (−0.1 to 0.42)	<b>+0.26</b> (0.01 to 0.50)
348PPM	+0.16 (−0.09 to 0.42)	<b>+0.24</b> (0.004 to 0.48)
300PPM	+0.15 (−0.09 to 0.38)	<b>+0.24</b> (0.02 to 0.46)
SAME-ICE	+0.23 (−0.03 to 0.49)	<b>+0.26</b> (0.03 to 0.50)

Values in bold are statistically significant at 95 % level from Student's *t* test

+ trend signal indicates weakening of the HC in the latter period

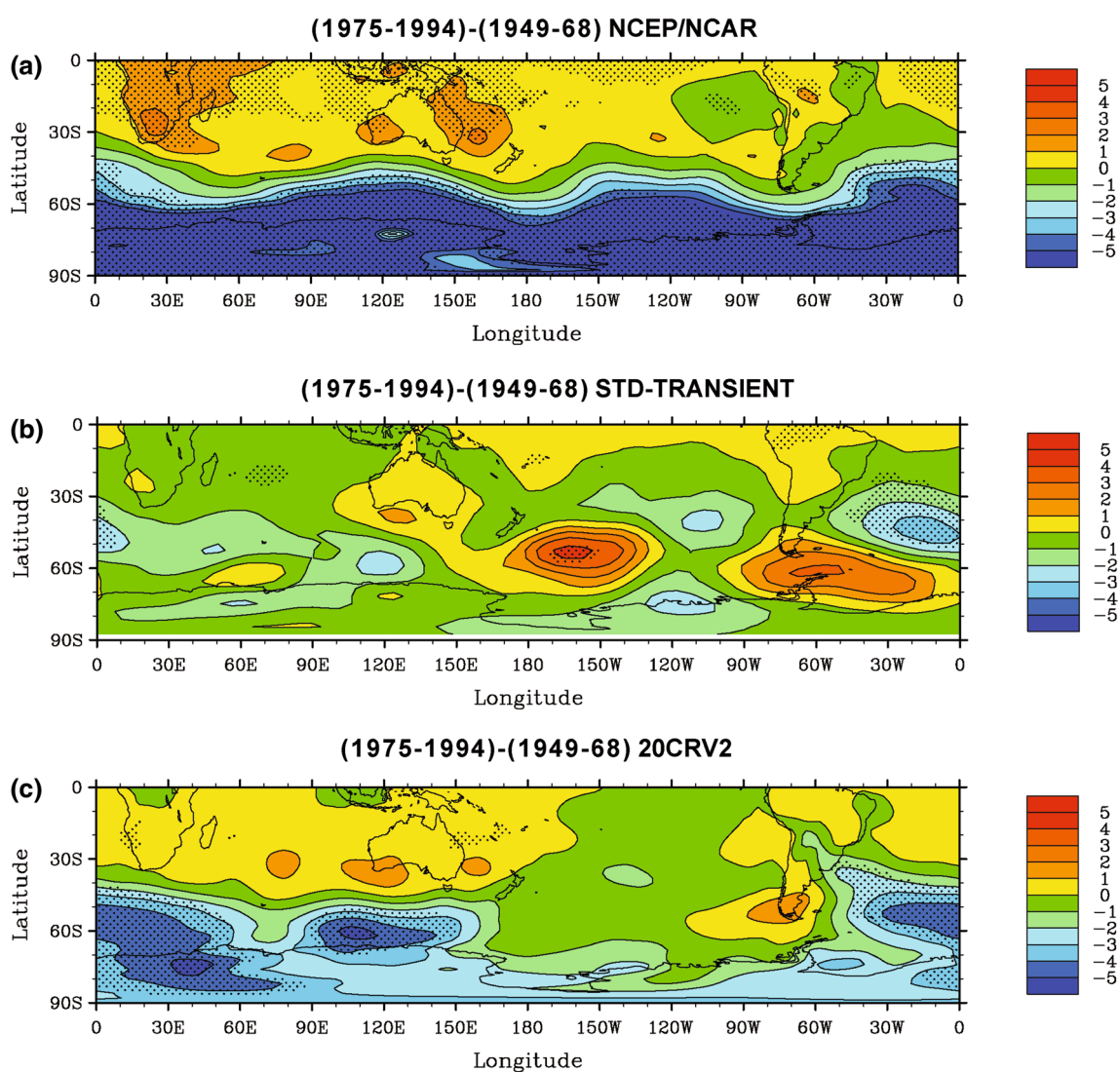


**Fig. 6** Sea level pressure (hPa) for the July difference (1975–1994)–(1949–1968). Plot **a** for the NCEP/NCAR data, **b** for the STD-TRANSIENT run and **c** for the 20CRV2 data. Contour intervals are

1 hPa with stippling indicating regions where the differences are statistically significant at the 95 % level as determined by Student's *t* test

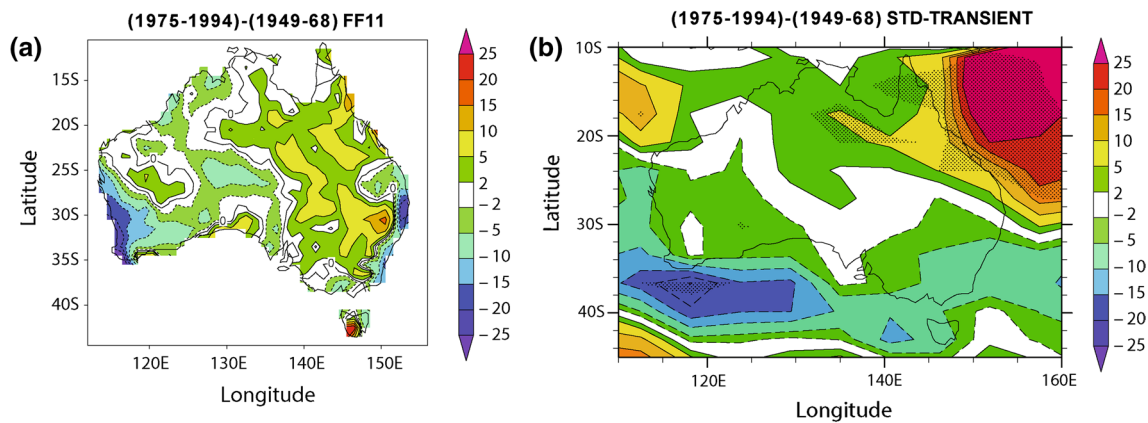


**Fig. 7** July Australian rainfall (mm/month) for the difference (1975–1994)–(1949–1968). Plot **a** obtained from Frederiksen and Frederiksen (2011) based on the Australian Bureau of Meteorological National Climate Centre mean gridded rainfall dataset (Jones and Weymouth 1997) and **b** for the STD-TRANSIENT run with stippling

indicating regions where the differences are statistically significant at the 90 % level as determined by Student's *t* test. Contour intervals are 5 mm/month. Negative (positive) values are indicated by *dashed* (*solid*) lines

in Perth mean sea level pressure (MSLP). Approximately 60 % of the variance in the SWWA winter rainfall is explained by fluctuations in Perth MSLP throughout the 1900s (FF05 and FF07).

Figure 6 shows the MSLP for the difference between the two periods (1949–1968) and (1975–1994). The reanalyses and the STD-TRANSIENT run show higher pressures at Perth for the latter period (1975–1994). However, the Perth MSLP changes are only significant in the NCEP/NCAR reanalysis. The reanalyses show different changes for the MSLP in the latter period over the central and eastern Pacific Ocean, but they agree better in the eastern hemisphere (Fig. 6a, c). The NCEP/NCAR reanalysis shows a significant hemispheric band of negative values south of 60°S. The STD-TRANSIENT simulation presents some aspects not observed in the reanalyses, such as the decrease of MSLP in the latter period over the Africa, Madagascar and the Indian Ocean, and a MSLP increase from 170°E to 130°W around 55°S. In the western hemisphere, specifically over the central Pacific, the model agrees better with the 20CRV2 (Fig. 6b, c). Differences between the model simulations and the reanalyses may be attributed to systematic model errors, decadal variability, the fact that the simulations do not explicitly include other greenhouse gases, as well as other natural and anthropogenic forcings, and errors in the reanalyses themselves.

### 3.5 Precipitation

Frederiksen and Frederiksen (2011, hereafter FF11) found large rainfall reductions in the 1975–1994 period over SWWA and eastern and southeastern Australia of around

20, 30, and 10 %, respectively (cf. Fig. 7a). FF05 and FF07 argued that this was related to a substantial reduction in the growth rate of leading storm modes developing over southwest Australia and upstream over the Indian Ocean near 30°S. These storms grow through baroclinic instability and a lessening in growth rates is associated with the atmosphere becoming more stable, or equivalently with a reduction in the vertical wind shear.

Figure 7b shows that the STD-TRANSIENT run captures some of the broad features of the rainfall reductions over the SWWA and eastern and south-eastern Australia, although with underestimated magnitude. The model also captures the rainfall increase over north-eastern and parts of central-north Australia. Frederiksen et al. (2011) performed an evaluation of twenty-two of the Coupled Model Intercomparison Project Three (CMIP3) models and showed that very few models were able to simulate the observed changes in rainfall for the 1975–1994 period. A significant advantage of the coupled general circulation models (CGCM) is that they simulate, as in the real world, the influence of the ocean on the overlying atmosphere and its response to fluctuations in surface heat fluxes driven by atmospheric variability. They also contain both the direct effects of anthropogenic CO<sub>2</sub> forcing (via differential changes in atmospheric heating) and the indirect effects (via changes in SST). However, their SST response (and especially the regional details of their SST response) may differ from the observed SST evolution, thereby affecting the fidelity of the simulated circulation (Deser and Phillips 2009). On the other hand, the AGCM with prescribed SST has the issue of the lack of coupling with an underlying ocean, which can also limit its skill to properly reproduce the observed changes.

#### 4 Contributions of forced and un-forced components in driving the climate shift

In this section we firstly analyse the atmospheric simulations (ensemble mean) with fixed and time-varying CO<sub>2</sub> concentrations to examine the role of the direct radiative forcing due to CO<sub>2</sub> in driving the inter-decadal changes found by FF05 and FF07 in the jet streams, temperature, Hadley circulation, mean sea level pressure and precipitation. In the Sect. 4.2 we also investigate the differences between the simulations forced with the same and different time evolving sea ice boundary conditions. The relative magnitude of the SST-forced and internal variability components is quantified in Sect. 4.3. Finally, in the Sect. 4.4 we analyse the observed changes in the SSTs using a non-stationary cluster analysis method.

##### 4.1 Simulations with fixed and time-varying CO<sub>2</sub> concentrations

The comparison of the inter-decadal changes in the jet streams between the TRANSIENT ensemble mean, which has historical time-evolving CO<sub>2</sub> concentration, and the 348PPM ensemble mean, which has fixed CO<sub>2</sub> concentration, allows us to evaluate the direct effect of the time-varying external radiative forcing due to CO<sub>2</sub>. Figure 8a, b indicate that the inclusion of the time-evolving CO<sub>2</sub> concentration does indeed have a direct effect. In the SH (NH), the magnitude of the zonal wind changes is larger (smaller) compared to the simulations without time-varying external forcing. The opposite behaviour in the two hemispheres is intriguing and demonstrates that the response of the NH and the SH circulation to the time evolution of CO<sub>2</sub> concentrations can be different. In this context, Grise and Polvani (2014) decomposed the atmospheric circulation response to CO<sub>2</sub> forcing into a direct component due to CO<sub>2</sub> radiative forcing and an indirect component associated with the SST changes and showed that, although well-mixed in the atmosphere, increasing CO<sub>2</sub> can drive very different circulation responses in the NH and SH.

The inclusion of the time-evolving CO<sub>2</sub> concentrations does not seem to have a great impact on the changes in the potential temperature at 500 hPa (Fig. 8c, d). In both cases, the significant warming south of 30°S, particularly in the eastern hemisphere, is reproduced. This is an indication that the effects of time-varying CO<sub>2</sub> concentrations are implicitly included in the SST signal. The changes in the atmospheric temperatures are also closely related to changes in the SSTs between the two periods (1949–1968) and (1975–1994) as shown in Fig. 9. This is particularly evident for the SST over the Indian Ocean around 30°S (Fig. 9a) and for the atmospheric potential temperature south of 30°S (Fig. 9b), where an increase is seen in the latter

period. When we perform the zonal mean of Fig. 9a, b, mostly positive differences from equator to pole are noted, clearly indicating this atmospheric and oceanic temperature increase (Fig. 9c), which results in a reduction in the latitudinal temperature gradient for the latter period. We expect that the increasing CO<sub>2</sub> concentration would have made a contribution to the changing SSTs. This indirect effect, associated with the SST changes, is discussed in more detail in Sect. 4.4.

The inclusion of the time-evolving CO<sub>2</sub> concentration does not seem to have a direct effect on the changes of the HC in the latter period. This is evident from the results shown in Table 2, i.e. a HC weakening of  $0.82 \times 10^9 \text{ kg s}^{-1}$  for the TRANSIENT ensemble mean and as well for the 348PPM ensemble mean. When we analyze each period and not just the difference between them, we see that the HC intensity in the 348PPM ensemble mean is a little weaker in both periods than the TRANSIENT ensemble mean, which has historical time-evolving CO<sub>2</sub> concentration. However, this difference for each period between the ensemble means is not statistically significant. Simulations with a different fixed CO<sub>2</sub> concentration (300 ppm) have also been performed to examine the sensitivity to the prescribed CO<sub>2</sub>. The mean CO<sub>2</sub> concentration for the 1949–1968 (1975–1994) basic state is about 316 (345) ppm. Thus, the concentration used in the 348PPM (300PPM) ensemble mean is larger (smaller) than the mean concentration for both periods. Table 2 shows that the 300PPM ensemble mean also presents a weakening of the HC around  $0.8 \times 10^9 \text{ kg s}^{-1}$  in the latter period. However, the HC intensity in the 300PPM ensemble mean is a little stronger (but still not significant) in both periods compared with the TRANSIENT and 348PPM ensemble means. Since the differences between the TRANSIENT, 348PPM and 300PPM ensemble means are not statistically significant we cannot state that there is a direct effect of time-evolving changes in CO<sub>2</sub> concentrations. The linear trend for July and for the JJA in the 1949–1994 period also shows a weakening of HC and almost no difference between the ensemble means (Table 3).

The main differences in the 1975–1994 period for the MSLP field between the TRANSIENT and the 348PPM ensemble means over the Australian continent are not statistically significant (figures not shown). As well, over most of the statistically significant regions (especially over the Indian and Atlantic Oceans) the changes are similar for the ensemble means. Therefore, we cannot state that there is an observed direct effect due to CO<sub>2</sub> for the MSLP field.

The TRANSIENT ensemble mean shows rainfall reductions only over the southern most parts of southwest and southeast Australia and over the ocean to the south where they are statistically significant (Fig. 8e). The 348PPM

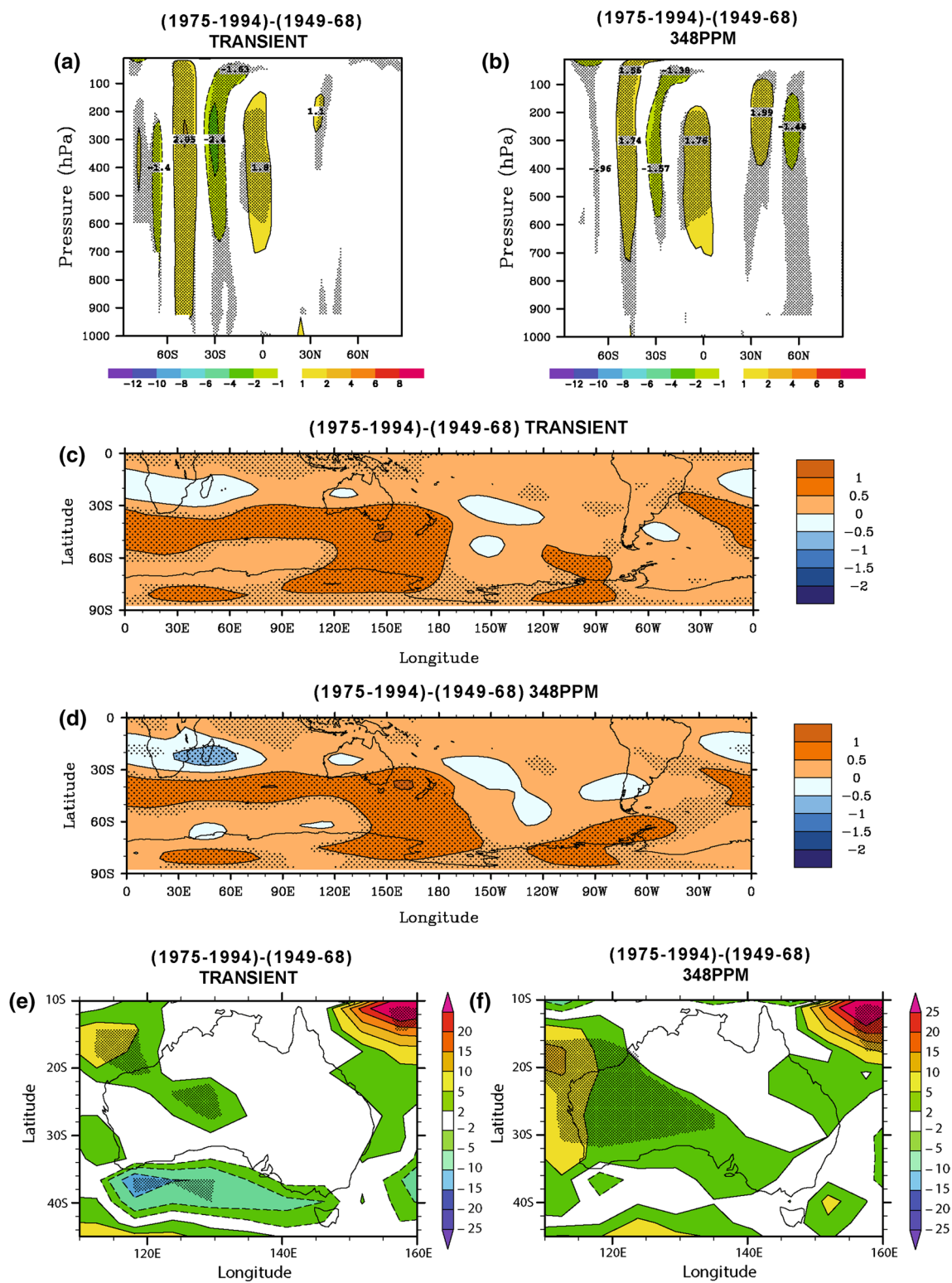


**Fig. 8** Vertical cross-section of July zonal wind ( $\text{m s}^{-1}$ ) for the difference (1975–1994)–(1949–1968) averaged between  $100^\circ$  and  $130^\circ\text{E}$  as a function of latitude and pressure (hPa) for the ensemble means: **a** TRANSIENT and **b** 348PPM. Potential temperature (K) for July at 500 hPa for the difference (1975–1994)–(1949–1968): **c** TRANSIENT and **d** 348PPM. July Australian rainfall (mm/month)

for the difference (1975–1994)–(1949–1968): **e** TRANSIENT and **f** 348PPM. Contour intervals are  $2 \text{ m s}^{-1}$  for (a) and (b),  $0.5 \text{ K}$  for (c) and (d), and  $5 \text{ mm/month}$  for (e) and (f). Stippling indicates regions where the differences are statistically significant at the 95 % (90 % for rainfall) level as determined by Student’s *t* test

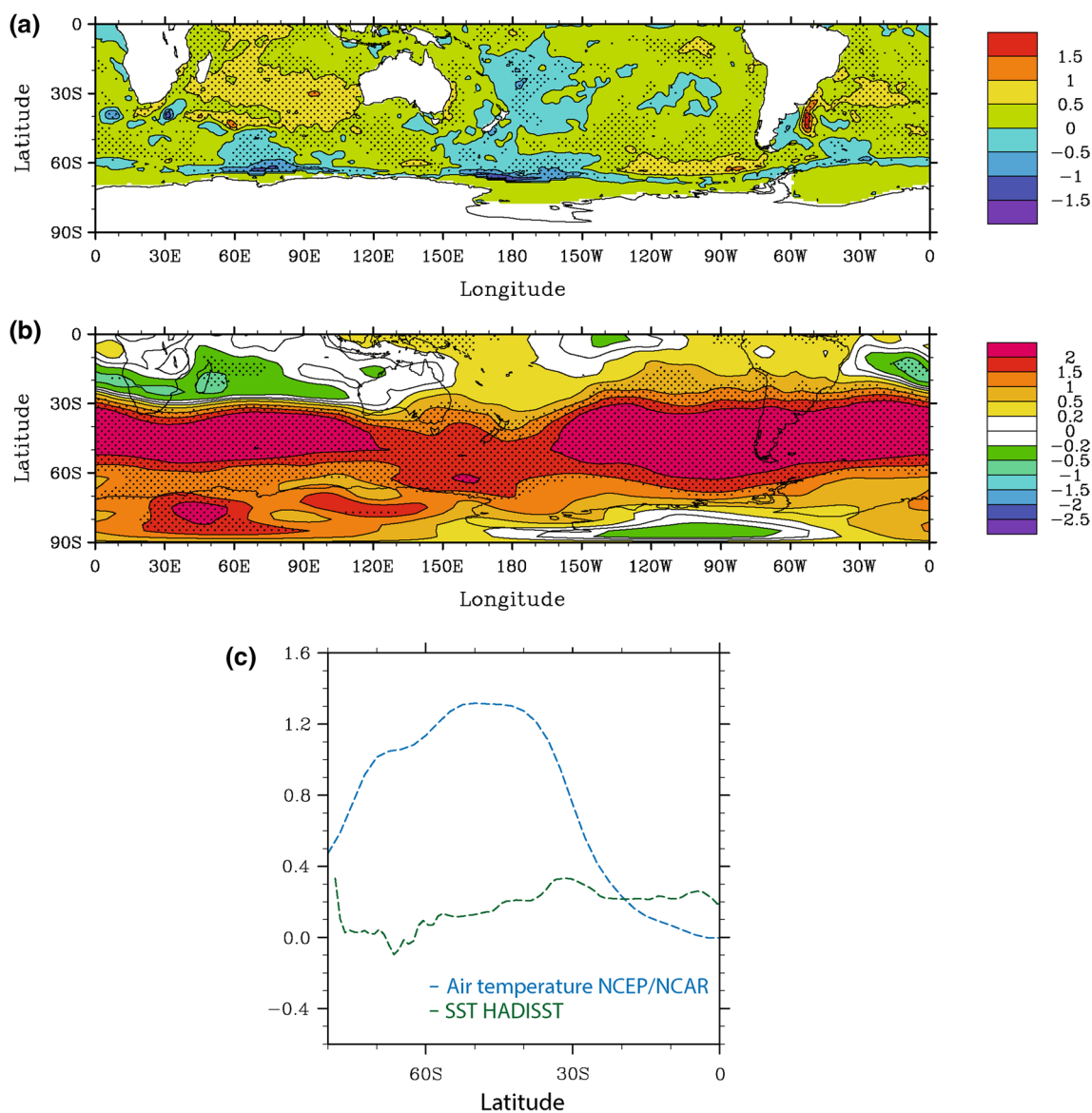


**Fig. 9** **a** July sea surface temperature (K) based on the HADISST dataset for the difference (1975–1994)–(1949–1968); **b** July potential temperature (K) based on the NCEP/NCAR reanalysis averaged on 700 hPa and 300 hPa pressure levels for the difference (1975–1994)–(1949–1968); **c** July zonal mean air temperature (SST) from NCEP/

NCAR (HADISST) for the difference (1975–1994)–(1949–1968). *Blue (green) line* corresponds to air temperature (SST). Contour intervals are 0.5 K for **(a)** and **(b)** with stippling indicating regions where the differences are statistically significant at the 95 % level as determined by Student's *t* test

ensemble mean shows only a small region with rainfall reduction over the ocean to the south of SWWA (Fig. 8f). The precipitation field in the TRANSIENT and the 348PPM ensemble means is quite similar in the subtropics, but over the southern Australia and further south large differences are seen, which are related to the similar differences in the jet streams (Fig. 8a, b).

In summary, the results have shown that there is little impact of the direct CO<sub>2</sub> radiative forcing on the changes in the 1975–1994 period, especially for the potential

temperature at 500 hPa, MSLP field and HC. However, the inclusion of the time-evolving CO<sub>2</sub> concentration has shown that there is sensitivity to the CO<sub>2</sub> emission trajectory for the precipitation field over southern Australia and further south. As well, in the SH (NH) the magnitude of the zonal wind changes is larger (smaller) compared to the simulations without time-varying external forcing. The results have also shown clearly that the atmospheric simulations with historical time-evolving CO<sub>2</sub> are more skilful in reproducing the inter-decadal changes.

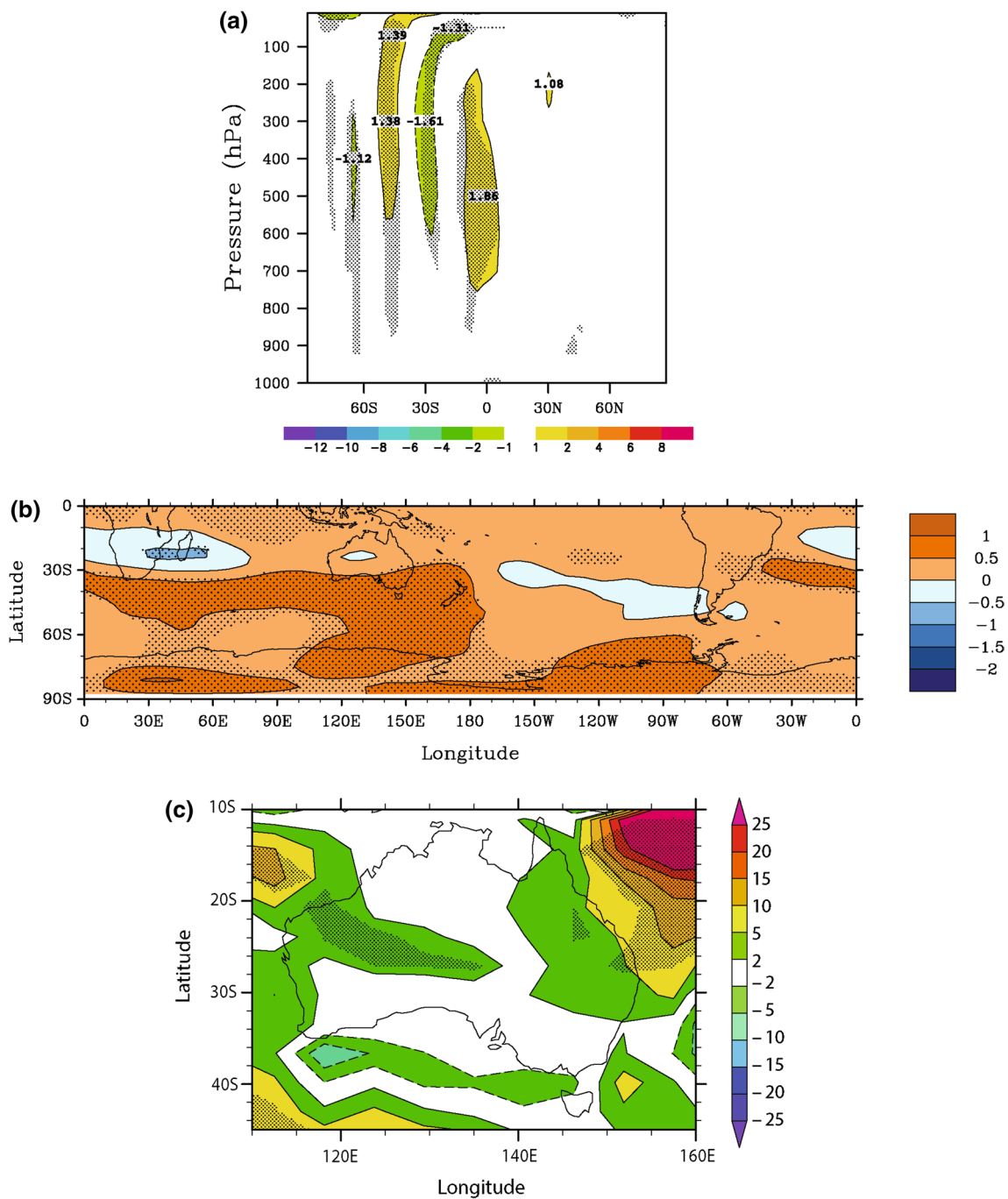


**Fig. 10** The difference (1975–1994)–(1949–1968) for the SAME-ICE ensemble mean. Plot **a** for vertical cross-section of July zonal wind ( $\text{m s}^{-1}$ ) averaged between  $100^\circ$  and  $130^\circ\text{E}$  as a function of latitude and pressure (hPa), **b** for potential temperature (K) for July at

500 hPa and **c** for July Australian rainfall (mm/month). Contour intervals are  $2 \text{ m s}^{-1}$  for **a**,  $0.5 \text{ K}$  for **b**, and  $5 \text{ mm/month}$  for **c**. Stippling indicates regions where the differences are statistically significant at the 95 % (90 % for rainfall) level as determined by Student's  $t$  test

#### 4.2 Simulations forced by the same sea ice boundary condition

Each member of the TRANSIENT ensemble began with slightly different initial conditions and is forced with the same time-varying observed SST and historical

time-evolving  $\text{CO}_2$  concentrations, but different sea ice boundary conditions (whose evolution is determined by the multi-layer dynamic-thermodynamic sea ice model). Here we test the hypothesis that the inter-decadal changes considered in this work may be significantly different when the ensemble members are constructed in the same way as

TRANSIENT runs but forced with the same time evolving sea ice boundary conditions (whose evolution is specified by the daily values of the STD-TRANSIENT run) in each realization. Thus, in the SAME-ICE experiment, the ensemble members only differ in their initial conditions.

The SAME-ICE ensemble mean shows a smaller magnitude of the zonal wind changes in both hemispheres for the latter period (Fig. 10a) compared with the TRANSIENT ensemble mean (Fig. 8a). Simmonds and Budd (1991) studied the sensitivity of the SH circulation to sea ice concentration and found that decreased sea ice concentration is associated with a warming of the troposphere and a weakening of westerlies. Therefore, in a scenario of sea ice concentration changes, alterations in the albedo over sea ice and in the incoming solar radiation are expected, resulting in zonal winds changes as reported by the authors. We investigated if there are changes in the sea ice concentration between the SAME-ICE and the TRANSIENT ensemble means. We found that around 60°S the sea ice concentration for the TRANSIENT ensemble mean is a little larger (around 1.2 % for the zonal mean) than for the SAME-ICE ensemble mean in the 1949–1994 period (figure not shown). In general, there is little difference between the SAME-ICE and the TRANSIENT ensemble means for the potential temperature at 500 hPa (Figs. 8c, 10b), the HC (Tables 2, 3), the MSLP (figure not shown since the main differences between the two periods are not statistically significant) and the precipitation (Figs. 8e, 10c), despite some local differences. In summary, these results implies that prescribing the same time evolving sea ice boundary conditions, i.e. removing the sea ice variability, does not greatly affects the large-scale flow inter-decadal changes.

### 4.3 Potential predictability

Diagnosing the contributions to atmospheric variability by external forcing and internal dynamics is exceedingly difficult in the real atmosphere partly because their effects are inextricably confounded and partly because of inhomogeneities in the observational data (Rowell and Zwiers 1999). However, it becomes possible using an ensemble of climate simulations, where all are forced by the same observed time-varying SSTs but started from different initial atmospheric conditions. Here we use the analysis of variance (ANOVA) proposed by Rowell et al. (1995) and Rowell (1998) to quantify the relative magnitude of the SST forced and internal variability. The statistical details of this technique were also described by Scheffe (1959) and Searle et al. (1992), so we give only a brief overview here.

Consider an ensemble of  $n$  climate simulations, each of  $N$  years in length, each forced by the same varying SSTs, and each one differing from the others only by its initial atmospheric conditions. Let  $x_{ij}$  be a time mean of some

atmospheric variable or index, in year  $i$  ( $i = 1, \dots, N$ ) and run  $j$  ( $j = 1, \dots, n$ ). The statistical model for  $x_{ij}$  consists as the sum of two independent components:

$$x_{ij} = \mu_i + \varepsilon_{ij} \quad (4)$$

where  $\mu_i$  is the component of  $x_{ij}$  due to SST forcing (the variance of the  $\mu_i$  is  $\sigma_{SST}^2$ ); and  $\varepsilon_{ij}$  is due to internal variability (the variance of the  $\varepsilon_{ij}$  is  $\sigma_{INT}^2$ ). Two assumptions are made in the application of the statistical model described above. The first is that the  $\varepsilon_{ij}$ 's are all randomly and independently selected from the same population with zero mean. The second assumption is that the  $\mu_i$ 's are independently and identically distributed random variables from some defined population.

Since each ensemble member is subject to the same boundary conditions, the spread among the members gives an unbiased estimate of the internal variability. In theory, if the size of the ensemble from a perfect model is infinite, the internal variability will be zero in the ensemble mean. However, in practice, it is impossible to generate an infinite ensemble set. Therefore, following Scheffe (1959), the SST forced variability ( $\sigma_{SST}^2$ ) can be deduced from the variance of the ensemble mean ( $\sigma_{EM}^2$ ) after removing the bias due to internal variability ( $\sigma_{INT}^2$ ).

$$\sigma_{SST}^2 = \sigma_{EM}^2 - \frac{1}{n}\sigma_{INT}^2 \quad (5)$$

Therefore, the  $x_{ij}$ 's can be used to obtain unbiased estimates of  $\sigma_{INT}^2$  and  $\sigma_{SST}^2$ . The sum of these variance components provides an unbiased estimate of the total variance,  $\sigma_{TOT}^2$

$$\sigma_{TOT}^2 = \sigma_{SST}^2 + \sigma_{INT}^2 = \sigma_{EM}^2 + \frac{n-1}{n}\sigma_{INT}^2 \quad (6)$$

To evaluate where on the globe atmospheric variations are sufficiently affected by SST forcing it is necessary to calculate the potential predictability (PP), i.e. the level of predictability that could be achieved given perfect knowledge of the boundary conditions. The PP is defined by the ratio of SST forced variance to total variance ( $\sigma_{SST}^2/\sigma_{TOT}^2$ ) and varies between 0 and 100 %. To calculate its statistical significance a Fisher's  $F$  test is used with the null hypothesis being  $PP = 0$ .

Rowell et al. (1995) and Rowell (1998) applied the ANOVA technique to assess potential predictability at seasonal and monthly timescales, however, the authors noted that it can also prove useful as a general analysis tool for understanding natural climate variability and potential atmospheric predictability on any chosen time or space scale (e.g. Chen and Van Den Dool 1997). Here, as shown in Fig. 11, we have calculated the PP of each atmospheric field analysed for monthly (July), seasonal (JJA) and inter-decadal time scales for the TRANSIENT ensemble mean in the 1949–1994 period. The inter-decadal time series were

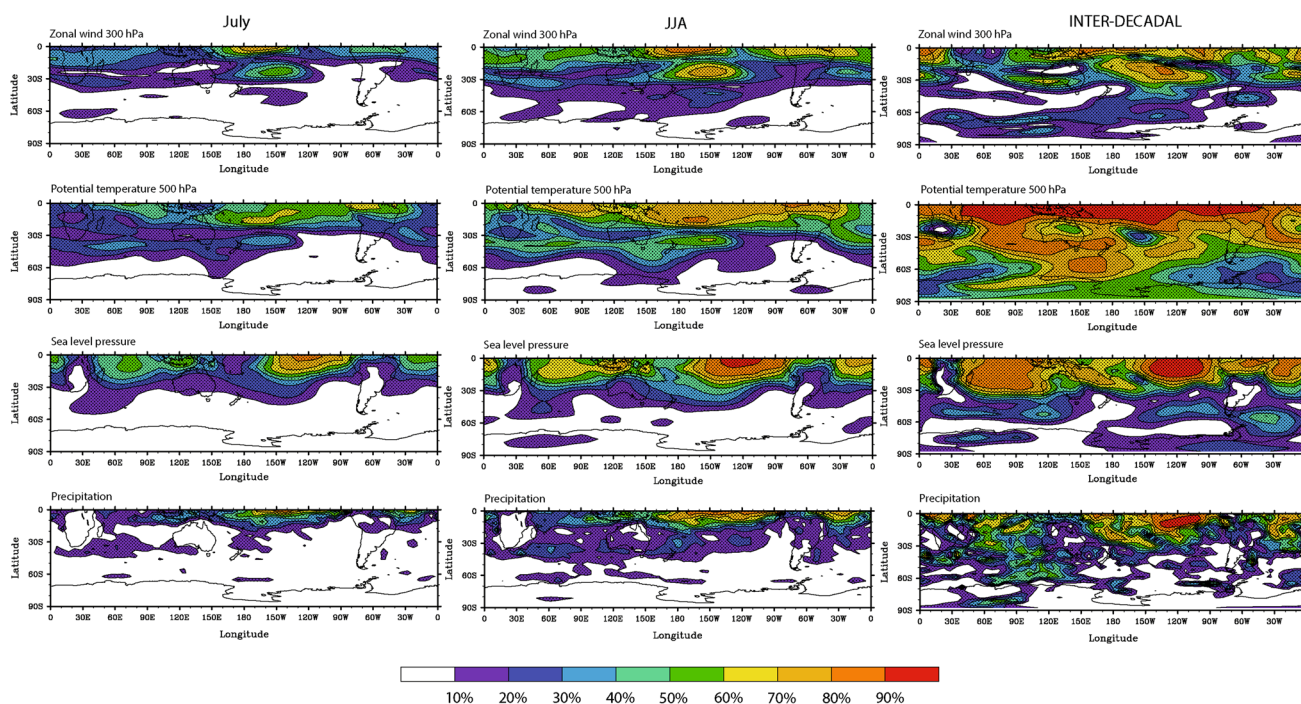


**Fig. 11** Potential predictability (%) for monthly (July), seasonal (JJA) and inter-decadal time scales of zonal wind at 300 hPa, potential temperature at 500 hPa, sea level pressure and precipitation for

the TRANSIENT ensemble mean in the 1949–1994 period. Regions where the potential predictability is greater than 10 % are significantly different from zero at the 99 % confidence level from an F-test

**Table 4** Area-averaged (AA) values of the potential predictability (PP) for the TRANSIENT ensemble mean in the 1949–1994 period

	PP July (%)	PP JJA (%)	PP Inter-decadal (Detrended annual time series) (%)
Zonal wind 300 hPa AA: 24°–30°S, 0°–360°E	<b>19.1</b>	<b>32.9</b>	<b>44.4 (43.9)</b>
Potential temperature 500 hPa AA: 30°–60°S and 0°–360°E	<b>13.9</b>	<b>25.6</b>	<b>63.8 (35.0)</b>
Sea level pressure AA: 112.5–118°E, 24°–37°S	<b>12.3</b>	<b>18.5</b>	<b>64.5 (52.5)</b>
Precipitation AA: 112.5–118°E, 24°–37°S	<b>10.4</b>	<b>17.9</b>	<b>33.6 (35.5)</b>

Values in bold are statistically significant at 99 % level from an F-test

computed by firstly calculating the annual mean of monthly data and then, smoothing the data by performing a 7-year running mean twice on the annual time series. The 7-year period is also used by other authors (e.g. Montecinos et al. 2003; Chen et al. 1996; Pizarro and Montecinos 2004; Dettinger and Diaz 2000) in order to filter out the interannual variations associated with El Niño-Southern Oscillation (ENSO), whose periodicities vary between 2 and 7 years. It is applied twice to eliminate residual high-frequency variability. After this processing the lengths of the records were reduced to 1955–1988 to remove possible end point effects of the filtering.

From Fig. 11, we note that on each time scale, lower values of PP are generally found in the extratropics since the forced to internal variance ratio ( $\sigma_{SST}^2/\sigma_{INT}^2$ ) is low due to

chaotic variability in the extratropics. In contrast, the variance ratio is high over the tropics where the SST forcing is dominant (cf. Rowell 1998). As well, we see that the PP values are higher primarily on the inter-decadal time scale and to a lesser extent on the seasonal time scale (JJA) than when we consider only the month of July. Rowell (1995) found that the internal variability was small at seasonal time scales, but not surprisingly becomes larger as one reduces either the spatial or temporal scale of analysis. Kumar and Hoerling (1995) noted that the effect of ensemble averaging may also be viewed to be equivalent to time averaging. The internal variance decreases with increasing ensemble size, thus time averaging on longer time scales should produce similar decrease in the internal variance. Therefore, when the intraseasonal variability is considered,

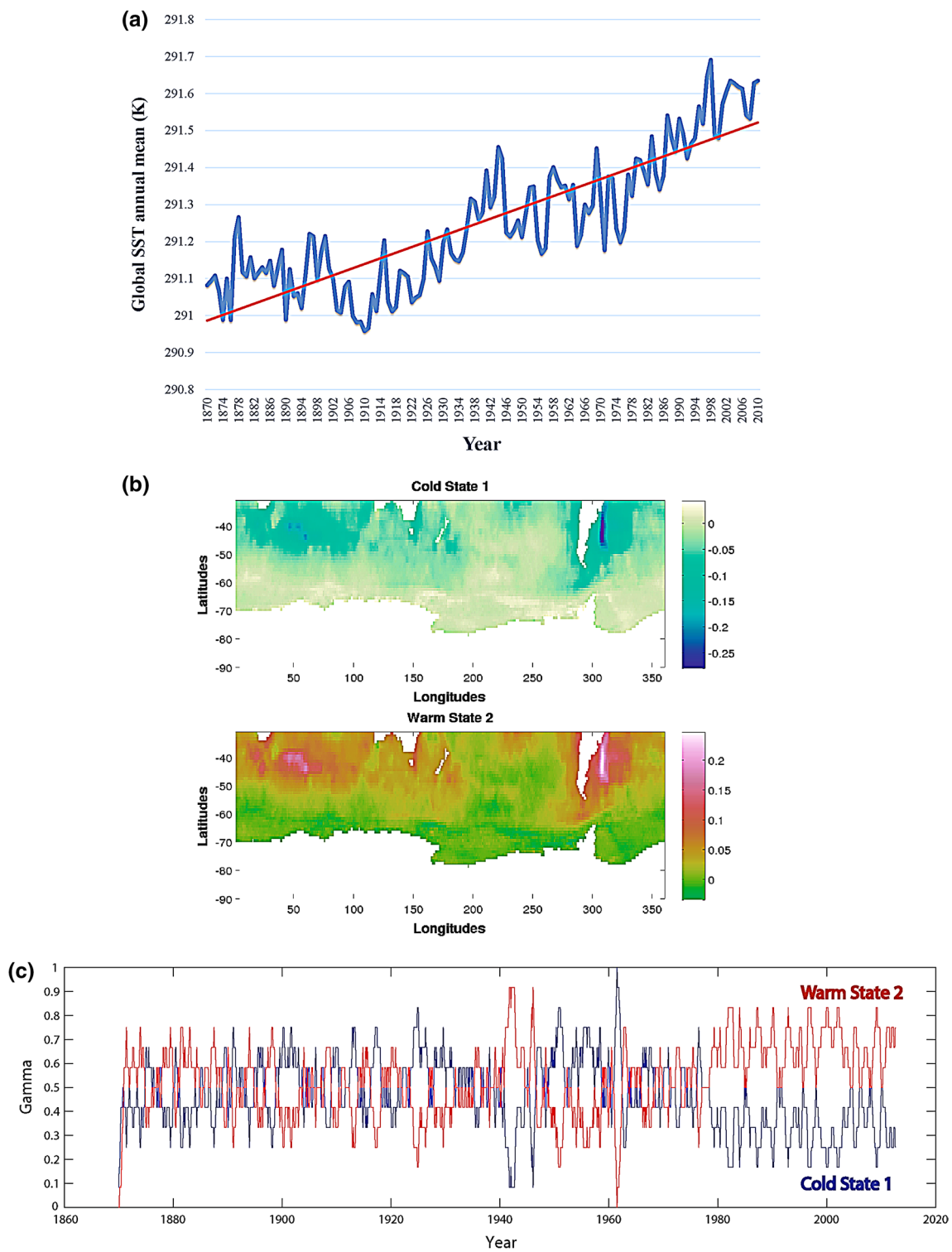


**Fig. 12** **a** Global sea surface temperature (K) annual mean for the period 1870–2010 based on the HADISST dataset with the linear trend line; **b** composite states from cluster analysis of HADISST data over the region south of 30°S: values greater than 0.1 or less

than  $-0.1$  are significant at the 95 % confidence level; **c** time series of gamma— $\gamma_i(t)$ , or model affiliation sequence, from cluster analysis of HADISST data with 12-month digital filter applied. *Blue (red) line* corresponds to cold state 1 (warm state 2)

the internal variance should increase and thus, the value of PP decreases.

Area-averages of the PP values for July, JJA and on the inter-decadal time scale have been calculated over the main regions of interest during the 1949–1994 period and the results are displayed in Table 4. For the zonal wind, the area considered is around the latitude of the Australian jet, which exhibited a strong reduction in the 1975–1994 period. The mid-latitude region is considered for potential temperature, since a significant warming was observed south of 30°S in the latter period. For MSLP and precipitation, the region around Perth is considered, since the main changes in these variables occurred in this region.

Montecinos et al. (2003) separated the very low frequency variability from the inter-decadal time scales by removing the linear trends of the annual time series before smoothing by twice applying a 7-year running mean. Here, we have also used their approach by employing the detrended-annual time series in the computation of the PP values at inter-decadal time scale. In this case, Table 4 shows a significant difference for the PP values of the extratropical zonal mean potential temperature at 500 hPa. This indicates an important contribution of the SST forced low frequency variability for the predictability of the extratropical potential temperature at 500 hPa. As discussed earlier, higher values of PP are found for the inter-decadal time scale (to the largest extent) and for the seasonal time scale (JJA) than when we consider only the month of July (Table 4). For July and JJA, the contribution of the SST forcing is greater for the zonal wind (hemispheric latitude band of 24°–30°S) at 300 hPa, whereas at inter-decadal time scale, the contribution is greater for the MSLP (region of 112.5–118°E, 24°–37°S). The internal variability of the atmosphere has an important role on the precipitation in the region 112.5–118°E, 24°–37°S for all time scales (especially in July).

#### 4.4 Changes in SSTs

The global and annual mean SST has broadly increased since 1870 with a significant positive trend of 0.04 °C per decade; the time series and the trend line based on the HADISST dataset are shown in Fig. 12a for the period 1870–2010. The increases in SST are suggestive of global warming associated with increasing greenhouse gases. We have made more detailed analyses of SST changes in the southern ocean south of 30°S using the nonstationary cluster analysis method summarised in the Appendix. We have focused on this extratropical region since it largely avoids the influence of tropical teleconnections associated with ENSO. The dimensionality of the dataset has been reduced by expanding it using principal component analysis (PCA) for the whole time period (January 1870–August 2012) and

retaining only the first 10 principal component time series in the analysis. The two leading cluster states are shown in Fig. 12b; they have essentially the same structure but with opposite signs, one warm and one cold relative to the background state. The warm state 2 corresponds to large scale warming of the southern ocean with enhanced warming of the western boundary currents—the East Australian Current, Brazil-Malvinas Confluence and the Agulhas Current. This pattern, and in particular the significant warming of the Indian Ocean and the Brazil-Malvinas Confluence, is in close agreement with the July SST difference pattern (south of 30°S) shown in Fig. 9a. In any given month the clustering associates the monthly mean HADISST data with one of either the warm or cold metastable regimes. The method finds the state that is most similar to the data and determines functions  $\gamma_i(t)$ ,  $i = 1, 2$ , where  $\gamma_1 + \gamma_2 = 1$ , which can be interpreted as probabilities that the data is in one or other of the two metastable states. The time series of  $\gamma_i(t)$  (or model affiliation sequence), filtered by a 12-month filter, shows the broad features and trends of the data between 1870 and 2012 (Fig. 12c).

We see that prior to about 1978 there was marked decadal variability but no particular preference for one state over the other. Post 1978 the system has a marked preference for the warm state, unlike the variability prior to this period. The papers of O’Kane et al. (2013a, b) showed that the entire Southern Ocean thermocline, as well as the boundary currents, underwent a systematic regime transition around 1978 associated with a more dominant positive phase of the Southern Annular Mode and a reduction in the persistence of the positive phase of the hemispheric wave-number three blocking pattern.

The transition between decadal variability and the preference for the warm SST state in the late 1970s suggests that the SST is carrying some of the signal of the CO<sub>2</sub> increase. We note that the changes in the July zonal winds and especially in the potential temperature (Fig. 8) between (1949–1968) and (1975–1994) are similar for the cases with increasing and with constant CO<sub>2</sub> concentration. The study of FF11 shows that the impact of further increases in CO<sub>2</sub> concentrations in skillful coupled ocean atmosphere CMIP3 models can lead to further changes in July zonal winds and reductions in SH baroclinicity near 30°S with trends during the twenty-first century similar to those during the second half of the twentieth century.

## 5 Discussion and conclusions

In this paper we first have investigated the skill of atmospheric simulations using the CSIRO Mk3L atmospheric model in reproducing important inter-decadal changes (first reported by FF05 and FF07) in the jet streams, temperature,

HC, MSLP and precipitation. The NCEP/NCAR reanalysis and the 20CRV2 dataset have been used for evaluation of the model simulations. We have focused on mean July climate fields for the periods 1949–1968 and 1975–1994. The difference between these two periods reflects the large changes that occurred during the climate shift in the mid-1970s.

Our results have shown that the simulations by the CSIRO Mk3L model with observed SSTs and historical time-evolving CO<sub>2</sub> concentration are quite skilful in reproducing the broad features of the following main observed changes in the NCEP/NCAR data that occurred in the latter period (1975–1994):

- In the upper troposphere: a reduction in the zonal wind near 30°S, an increase near 45°S and in the main NH jet core near 35°N;
- Significant warming south of 30°S, leading to a reduced equator-to-pole temperature gradient, particularly in the eastern hemisphere;
- Weakening of the HC;
- Increase in Perth MSLP;
- The rainfall reduction over SWWA and southeastern Australia (dataset of Jones and Weymouth 1997).

The 20CRV2 reproduces the inter-decadal changes in the jet streams, temperature and MSLP. However, in the case of the HC, the opposite change was found, which may be attributed mainly to differences in the regional HC in the latter period.

Our results have also shown that, for the periods considered in this work, the model simulations, and the NCEP/NCAR and 20CRV2 reanalyses, agree in the eastern hemisphere, but in the western hemisphere, the reanalyses show significant differences with the model simulations combining aspects of these two datasets. Differences between the reanalyses may be attributed to differences in the data assimilation techniques utilized. For example, for the 20CRV2 dataset only surface pressure observations are assimilated while for the NCEP/NCAR reanalysis other available atmospheric fields have also been employed. Differences between the model simulations and the reanalyses may be attributed to systematic model errors, decadal variability, the fact that the simulations do not explicitly include other greenhouse gases, as well as other natural and anthropogenic forcings, and errors in the reanalyses themselves.

In the second part of this study, we investigated the role of the direct radiative forcing due to CO<sub>2</sub> in driving the inter-decadal changes. The results have shown that there is little impact of the direct CO<sub>2</sub> radiative forcing on the changes in the 1975–1994 period, once the indirect effect of changing SSTs is taken into account, especially for the potential temperature at 500 hPa, MSLP field and HC.

However, the inclusion of the time-evolving CO<sub>2</sub> concentration showed that there is sensitivity to the CO<sub>2</sub> emission trajectory for the precipitation field over southern Australia and further south. As well, in the SH (NH) the magnitude of the zonal wind changes is larger (smaller) compared with the simulations without time-varying external forcing. Our simulations with fixed CO<sub>2</sub> concentration have also shown clearly that the atmospheric simulations with historical time-evolving CO<sub>2</sub> are more skilful in reproducing the inter-decadal changes. This was also noted by Folland et al. (1998), who found that the inclusion of changes in other forcing factors results in simulations that are significantly closer to the observations than using SST variations alone.

The sensitivity of the results to the same sea ice boundary condition imposed in each realization has also been investigated. A small reduction in the sea ice concentration and the magnitude of the changes in the 1975–1994 period was found for the SH zonal wind, MSLP and precipitation fields for the simulations with the same sea ice. Therefore, prescribing the same sea ice boundary conditions, i.e. removing the sea ice variability, does not greatly affect the large-scale flow inter-decadal changes.

Non-stationary vector autoregressive clustering techniques have shown that the southern ocean (south of 30°S) underwent a major regime transition in the late 1970s, and this transition was unlike the decadal variability of the preceding century. We are currently locked into a new regime where the Indian Ocean and western boundary currents are warming and this is unprecedented in the recent past. A reduction in the SST gradient is consistent with a reduction in the atmospheric baroclinicity, as found here for the zonal wind in the latter period (1975–1994). We note that studies like Hansen and Lebedeff (1988) have found that the global surface air temperature substantially increased in the 1980s. Thus, it is reasonable to assume that these changes in the SST are not just due to the decadal variability, but have a contribution from increasing greenhouse gases.

The calculation of the potential predictability indicates that both external forcing, due to SST and atmospheric radiative alterations, and internal variability play significant roles in the inter-decadal SH large-scale atmospheric circulation changes that occurred in the mid-1970s. Deser and Phillips (2009) emphasized the importance of both sea surface temperature and atmospheric radiative changes in forcing global atmospheric circulation trends during 1950–2000. Folland et al. (1998), adopting a still broader perspective, stated that the climate change and variability we have seen over the last half century is the result of direct effects of the changing natural and anthropogenic forcing factors on atmospheric temperature and on the land surface, the indirect effect on climate of these factors through SST and sea-ice changes and internal atmospheric and oceanic variability that is independent of these forcing changes.

It is remarkable that the stand-alone atmospheric CSIRO Mk3L model forced by observed SST and CO<sub>2</sub> concentrations can skillfully reproduce many of the broad features of these changes, despite some differences, especially in the western hemisphere. In recent work that will be reported on in a separate study, we have examined the extent to which the climate shift persisted after the 1975–1994 period. FF11 noted that it continued during the 10 year period 1997–2006. We have also found that circulation anomalies, including reduction in the July jet stream maxima near 30°S, persisted for the length of the Australian Millennium Drought from 1997 to 2009. This is seen in both the NCEP/NCAR and 20CRV2 reanalyses and in simulations with the CSIRO Mk3L model, albeit with reduced magnitude.

**Acknowledgments** A.C.V. Freitas acknowledges São Paulo Research Foundation (FAPESP) for financial support (grant 2012/14231-1) and CSIRO Oceans and Atmosphere Flagship for technical support. T.J. O’Kane is supported by an Australian Research Council Future Fellowship. T. Ambrizzi had partial support from CNPq (Grant 300976/2010-0), FAPESP (Grant 2008/58101-9) and VALE Technology Association Institute (ITV-VALE). This work is partly supported by the Australian Government Department of Climate Change and Energy Efficiency. We are grateful to Steven Phipps for the assistance with the CSIRO Mk3L model. We thank the two reviewers whose insightful comments improved substantially an earlier version of the manuscript.

## Appendix: Clustering Methodology

We use monthly mean HADISST sea surface temperature data over the period January 1870–August 2012. The clustering analysis uses the Finite Element Method (FEM) with Bounded Variation (BV)-regularization and Vector Autoregressive Factor (VARX) models (FEM-BV-VARX) formulated by Horenko (2010) and employed by O’Kane et al. (2013a, b). Full details are given in Metzner et al. (2012) and O’Kane et al. (2013a, b). Briefly the approach assumes that the data set  $x_t$  may be represented by a stochastic model with memory effects and by fitting the parameters by a non-stationary stochastic (VARX) model of the form

$$x_t = \mu_\gamma(t) + \sum_{q=1}^m A_\gamma(t)x_{t-q\tau} + C_\gamma(t)\varepsilon_t \quad (7)$$

Here  $\varepsilon$  is a Gaussian process with zero mean,  $A$  and  $C$  are tensors,  $\mu$  is the mean,  $\tau$  is the time lag, and  $\gamma$  denotes the regime state. One might also consider external forcing factors but do not consider them here. The optimal number of cluster states  $K$  is determined on the basis of information theory through the Akaike Information Criterion (Horenko 2010; O’Kane et al. 2013a, b). The method simultaneously estimates the clusters (corresponding to regimes) and the most likely meta-stable state transitions between the clusters through the minimization of an average clustering

functional  $L$  of a given high-dimensional time series. This approach assumes that the dynamics of the observed variable of interest  $x_t$  is influenced by the previous  $m$  time-lagged values of the same variable (to describe the memory effects) and an unobservable (hidden) stochastic variable  $\varepsilon$  associated with regime transitions that strongly influences the observed variable. Before applying the clustering algorithm we decompose the HADISST anomalies (seasonal cycle subtracted) into Empirical Orthogonal Functions (EOFs) and then use the leading 10 EOFs for the clustering.

## References

- Allan RJ, Haylock MR (1993) Circulation features associated with the winter rainfall decrease in south-western Australia. *J Clim* 6:1356–1367
- Archer CL, Caldeira K (2008) Historical trends in the jet streams. *Geophys Res Lett* 35:L08803
- Baines PG (2005) Long-term variations in winter rainfall of southwest Australia and the African monsoon. *Aust Met Mag* 54:91–102
- Bracco A, Kucharski F, Kallummal R, Molteni F (2004) Internal variability, external forcing and climate trends in multi-decadal AGCM ensembles. *Clim Dyn* 23:659–678
- Cash BA, Schneider EK, Bengtsson L (2005) Origin of regional climate differences: role of boundary conditions and model formulation in two GCMs. *Clim Dyn* 25:709–723
- Chen WY, Van Den Dool HM (1997) Atmospheric predictability of seasonal, annual, and decadal climate means and the role of the ENSO cycle: a model study. *J Clim* 10:1236–1254
- Chen T-C, Chen J-M, Wikle CK (1996) Interdecadal variation in U.S. Pacific Coast precipitation over the past four decades. *Bull Am Meteor Soc* 77(6):1197–1205
- Chen H, Schneider EK, Kirtman BP, Colfescu I (2013) Evaluation of weather noise and its role in climate model simulations. *J Clim* 26:3766–3784
- Compo GP, Whitaker JS, Sardeshmukh PD et al (2011) The twentieth century reanalysis project. *Q J R Meteorol Soc* 137:1–28
- Deser C, Phillips AS (2009) Atmospheric circulation trends, 1950–2000: the relative roles of sea surface temperature forcing and direct atmospheric radiative forcing. *J Clim* 22:396–413
- Dettinger MD, Diaz HF (2000) Global characteristics of stream flow seasonality and variability. *J Hydrometeorol* 1:289–310
- Folland CK et al (1998) Influences of anthropogenic and oceanic forcing on recent climate change. *Geophys Res Lett* 25:353–356
- Frederiksen JS and Frederiksen CS (2005) Decadal changes in Southern Hemisphere winter cyclogenesis, CSIRO Marine and Atmospheric research paper; 002, Aspendale, Vic.: CSIRO Marine and Atmospheric Research. V. [http://www.cmar.csiro.au/e-print/open/frederiksenjs\\_2005b.pdf](http://www.cmar.csiro.au/e-print/open/frederiksenjs_2005b.pdf). 29 pp. Accessed 15 May 2014
- Frederiksen JS, Frederiksen CS (2007) Inter-decadal changes in southern hemisphere winter storm track modes. *Tellus A* 59:599–617
- Frederiksen JS, Frederiksen CS (2011) Twentieth century winter changes in Southern Hemisphere synoptic weather modes. *Adv Meteorol* 353829:1–16. doi:10.1155/2011/353829
- Frederiksen CS, Frederiksen JS, Sissons JM, Osbrough SL (2011) Changes and projections in Australian winter rainfall and circulation: anthropogenic forcing and internal variability. *Int J Clim Change Impacts and Responses* 2:143–162
- Gastineau G, Li L, Le Treut H (2009) The hadley and walker circulation changes in global warming conditions described by idealized atmospheric simulations. *J Clim* 22:3993–4013

- Gordon HB, Rotstayn LD, McGregor JL et al (2002) The CSIRO Mk3 climate system model, Technical Paper 60, CSIRO Atmospheric Research
- Gregory D, Rowntree PR (1990) A mass flux convection scheme with representation of cloud ensemble characteristics and stability-dependent closure. *Mon Wea Rev* 118:1483–1506
- Grimm AM, Sahai AK, Ropelewski CF (2006) Inter-decadal variations in AGCM simulation skills. *J Clim* 19:3406–3419
- Grise KM, Polvani LM (2014) The response of midlatitude jets to increased CO<sub>2</sub>: distinguishing the roles of sea surface temperature and direct radiative forcing. *Geophys Res Lett* 41:6863–6871
- Hansen J, Lebedeff S (1988) Global surface air temperatures: update through 1987. *Geophys Res Lett* 15:323–326
- Holton RJ (2004) An introduction to dynamic meteorology, 4th edn. Elsevier/Academic Press, Waltham, p 535
- Hope PK, Drosowsky W, Nicholls N (2006) Shifts in the synoptic systems influencing southwest Western Australia. *Clim Dyn* 26:751–764
- Horenko I (2010) Finite element approach to clustering of multidimensional time series. *SIAM J Sci Comput* 32:62–83
- Jones DA, Weymouth G (1997) An Australian monthly rainfall data set, Tech. Rep. 70, p. 19, Bureau of Meteorology, Australia
- Kalnay E, Kanamitsu M, Kistler R et al (1996) The NCEP/NCAR 40 year reanalysis project. *Bull Am Meteor Soc* 77:437–471
- Kumar A, Hoerling MP (1995) Prospects and limitations of seasonal atmospheric GCM predictions. *Bull Am Meteor Soc* 76:335–345
- Lucas C, Timbal B, Nguyen H (2014) The expanding tropics: a critical assessment of the observational and modeling studies. *WIREs Clim Change* 5:89–112
- Meehl GA, Washington WM, Ammann CM, Arblaster JM, Wigley TML, Tebaldi C (2004) Combinations of natural and anthropogenic forcings in twentieth-century climate. *J Clim* 17:3721–3727
- Meehl GA, Hu A, Santer BD (2009) The Mid-1970s climate shift in the Pacific and the relative roles of forced versus inherent decadal variability. *J Clim* 22:780–792
- Meng Q, Latif M, Park W, Keenlyside NS, Semenov VA, Martin T (2012) Twentieth century Walker circulation change: data analysis and model experiments. *Clim Dyn* 38:1757–1773
- Metzner P, Putzig L, Horenko I (2012) Analysis of persistent non-stationary time series and applications. *Comm App Math Comp Sci* 7:175229
- Montecinos A, Purca S, Pizarro O (2003) Interannual-to-interdecadal sea surface temperature variability along the western coast of South America. *Geophys Res Lett* 30:1–4. doi:10.1029/2003GL017345
- Nitta T, Yamada S (1989) Recent warming of tropical sea surface temperature and its relationship to the Northern Hemisphere circulation. *J Meteor Soc Jpn* 67:375–383
- O’Kane TJ, Risbey JS, Franzke C, Horenko I, Monselesan DP (2013a) Changes in the metastability of the midlatitude southern hemisphere circulation and the utility of nonstationary cluster analysis and split-flow blocking indices as diagnostic tools. *J Atmos Sci* 70:824–842
- O’Kane TJ, Matear R, Chamberlain M, Risbey J, Sloyan B, Horenko I (2013b) Decadal variability in an OGCM Southern Ocean: intrinsic modes, forced modes and metastable states. *Ocean Model* 69:121
- Oort AH, Yienger JJ (1996) Observed interannual variability in the Hadley circulation and its connection to ENSO. *J Clim* 9:2751–2767
- Pena-Ortiz C, Gallego D, Ribera P, Ordóñez P, Alvarez-Castro MDC (2013) Observed trends in the global jet stream characteristics during the second half of the 20th century. *J Geophys Res Atmos* 118:2702–2713
- Pezza AB, Durrant T, Simmonds I, Smith I (2008) Southern Hemisphere synoptic behaviour in extreme phases of SAM, ENSO, sea ice extent, and southern Australia rainfall. *J Clim* 21:5566–5584
- Phipps SJ (2010) The CSIRO Mk3L climate system model v1.2, Technical Report No. 4, Antarctic Climate & Ecosystems CRC, Hobart, Tasmania, Australia, 121 pp., ISBN 978-1-921197-04-8
- Phipps SJ, Rotstayn LD, Gordon HB, Roberts JL, Hirst AC, Budd WF (2011) The CSIRO Mk3L climate system model version 1.0 - Part 1: description and evaluation. *Geosci Model Dev* 4:483–509. doi:10.5194/gmd-4-483-2011
- Phipps SJ, McGregor HV, Gergis J, Gallant AJE, Neukom R, Stevenson S, Ackerley D, Brown JR, Fischer MJ, van Ommen TD (2013) Paleoclimate data-model comparison and the role of climate forcings over the past 1500 years. *J Clim* 26:6915–6936. doi:10.1175/JCLI-D-12-00108.1
- Pizarro O, Montecinos A (2004) Interdecadal variability of the thermocline along the west coast of South America. *Geophys Res Lett* 31(L20307):1–5. doi:10.1029/2004GL020998
- Pook MJ, Risbey JS, McIntosh PC (2012) The synoptic climatology of cool-season rainfall in the central wheatbelt of Western Australia. *Mon Wea Rev* 140:28–43
- Rayner NA, Parker DE, Horton EB, Folland CK, Alexander LV, Rowell DP, Kent EC, Kaplan A (2003) Global analyses of sea surface temperature, sea ice, and night marine air temperature since the late nineteenth century. *J Geophys Res* 108:1–37
- Robert AJ (1966) The integration of a low order spectral form of the primitive meteorological equations. *J Meteorol Soc Japan* 44:237–244
- Rotstayn LD (1997) A physically based scheme for the treatment of stratiform clouds and precipitation in large-scale models. I: description and evaluation of the microphysical processes. *Q J R Meteorol Soc* 123:1227–1282
- Rotstayn LD (1998) A physically based scheme for the treatment of stratiform clouds and precipitation in large-scale models. II: comparison of modelled and observed climatological fields. *Q J R Meteorol Soc* 124:389–415
- Rotstayn LD (2000) On the “tuning” of autoconversion parameterizations in climate models. *J Geophys Res* 105:15495–15507
- Rowell DP (1998) Assessing potential seasonal predictability with an ensemble of multidecadal GCM simulations. *J Clim* 11:109–120
- Rowell DP, Zwiers FW (1999) The global distribution of sources of atmospheric decadal variability and mechanisms over the tropical Pacific and southern North America. *Clim Dyn* 15:751–772
- Rowell DP, Folland CK, Maskell K, Ward MN (1995) Variability of summer rainfall over tropical north Africa (1906–1992): observations and modelling. *Q J R Meteorol Soc* 121:669–704
- Sadler BS, Mauger GW and Stokes RA (1988) The water resources implications of a drying climate in south-west Western Australia. In: G.I. Pearman (ed) *Greenhouse: Planning for Climate Change*, 296–311. Commonwealth Scientific and Industrial Research Organization, Australia, 752 pp
- Scheffe H (1959) *The analysis of variance*. Wiley, New York, p 477
- Searle SR, Casella G, McCulloch CE (1992) *Variance components*. Wiley, New York 501 pp
- Shukla J (1981) Dynamical predictability of monthly means. *J Atmos Sci* 38:2547–2572
- Simmonds I, Budd WF (1991) Sensitivity of the southern hemisphere circulation to leads in the Antarctic pack ice. *Q J Roy Meteor Soc* 113:1003–1024
- Smith IN, McIntosh P, Ansell TJ, Reason CJC, McInnes K (2000) South-west Western Australian winter rainfall and its association with Indian Ocean climate variability. *Int J Climatol* 20:1913–1930
- Song H, Zhang M (2007) Changes of the boreal winter Hadley Circulation in the NCEP–NCAR and ECMWF reanalyses: a comparative study. *J Clim* 20:5191–5200
- Stachnik JP, Schumacher C (2011) A comparison of the Hadley circulation in modern reanalyses. *J Geophys Res* 116:D22102. doi:10.1029/2011JD016677

- Stephenson DB, Held IM (1993) GCM response of northern winter stationary waves and storm tracks to increasing amounts of carbon dioxide. *J Clim* 6:1859–1870
- Tett SFB et al (1999) Causes of twentieth-century temperature change near the Earth's surface. *Nature* 399:569–572
- Wang W-C, Liang X-Z, Dudek MP, Pollard D, Thompson SL (1995) Atmospheric ozone as a climate gas. *Atmos Res* 37:247–256
- Zidikheri MJ, Frederiksen JS (2013) An efficient closure based method for inverse climate modelling. MODSIM 2013. 146–152. <http://www.mssanz.org.au/modsim2013/A2/zidikheri.pdf>. Accessed 15 May 2014